

© 2012 Tianjian Lu

SIGNAL INTEGRITY ANALYSIS OF HIGH-SPEED MULTILAYER  
INTERCONNECTS USING THE FINITE ELEMENT METHOD

BY

TIANJIAN LU

THESIS

Submitted in partial fulfillment of the requirements  
for the degree of Master of Science in Electrical and Computer Engineering  
in the Graduate College of the  
University of Illinois at Urbana-Champaign, 2012

Urbana, Illinois

Adviser:

Professor Jianming Jin

# ABSTRACT

Approaches of modeling high-speed interconnects generally fall into two categories: circuit models based on circuit-parameter extractions and full-wave methods based on solving Maxwell's equations. Even though computationally efficient, the approaches based on circuit-parameter extractions fail to provide accurate predictions due to the increased coupling and radiation effects at high frequencies. This work targets the fast and efficient full-wave analysis of high-speed multilayer interconnects. To enhance the efficiency of the full-wave analysis, fast frequency sweep techniques and domain decomposition schemes are first investigated and then implemented. This work consists of four major parts. (1) The full-wave analysis is implemented based on the finite element method. The capability of handling arbitrary geometries of the finite element method is utilized to deal with complex circuit structures. (2) The efficiency of the full-wave method is enhanced for broadband characterization by the incorporation of the solution space projection. (3) Various domain decomposition schemes are employed to break an originally large problem into smaller ones and allow the possibility of parallel computing. (4) The solution space projection and the domain decomposition schemes are combined in a mutually beneficial manner which achieves an even more efficient full-wave analysis.

*To my parents and Lin, for their endless love and support.*

# ACKNOWLEDGMENTS

I am very grateful to my advisor, Professor Jianming Jin, for his profound knowledge and expertise in leading me into this field and his constant motivation and inspiration not only toward the completion of this work but also in my life as a researcher.

I would also like to thank all my colleagues for their help and the fun they brought into my research life.

Last but not least, I would like to thank my parents and Ms. Lin Feng for their endless love and support over the years as I pursued my dream.

# TABLE OF CONTENTS

LIST OF FIGURES . . . . .	vi
CHAPTER 1 INTRODUCTION . . . . .	1
CHAPTER 2 THREE-DIMENSIONAL FINITE ELEMENT FOR-	
MULATION . . . . .	4
2.1 The Boundary Value Problem . . . . .	4
2.2 Absorbing Boundary Condition . . . . .	5
2.3 Wave Port . . . . .	8
2.4 Basis Functions . . . . .	11
CHAPTER 3 SOLUTION SPACE PROJECTION AND FAST	
FREQUENCY SWEEP . . . . .	16
3.1 Solution Space Projection . . . . .	16
3.2 Adaptive Multi-Point Scheme . . . . .	17
3.3 Numerical Examples . . . . .	18
CHAPTER 4 DOMAIN DECOMPOSITION OF THE MULTI-	
LAYER INTERCONNECTS . . . . .	31
4.1 Domain Decomposition by Layers: The Approximate Modal	
Interface Method . . . . .	32
4.2 The Approximate Modal Interface Method and the Solu-	
tion Space Projection . . . . .	39
4.3 Domain Decomposition within Layers: The Finite Element	
Tearing and Interconnecting . . . . .	41
4.4 The Finite Element Tearing and Interconnecting and the	
Solution Space Projection . . . . .	44
4.5 Numerical Examples . . . . .	44
CHAPTER 5 CONCLUSION . . . . .	55
REFERENCES . . . . .	57

# LIST OF FIGURES

2.1	Nodal basis functions on triangular element . . . . .	12
2.2	Edge basis functions on a triangular and tetrahedral element .	14
3.1	Coaxial transmission line . . . . .	19
3.2	S-parameters of lossy coaxial cable . . . . .	20
3.3	S-parameters of lossy coaxial cable . . . . .	21
3.4	S-parameters of lossy coaxial cable . . . . .	21
3.5	S-parameters of lossy coaxial cable . . . . .	22
3.6	Top view and front view . . . . .	23
3.7	S-parameters of a metal-loaded H-plane waveguide T-junction	23
3.8	Microstrip low-pass filter . . . . .	24
3.9	Insertion loss of a microstrip low-pass filter . . . . .	25
3.10	Return loss of a microstrip low-pass filter . . . . .	25
3.11	Microstrip branch line coupler . . . . .	26
3.12	S-parameters of microstrip branch line coupler . . . . .	27
3.13	Single via structure with two dielectric layers . . . . .	28
3.14	S-parameters of single via structure with $\theta = 180^\circ$ . . . . .	29
3.15	S-parameters of single via structure with $\theta = 90^\circ$ . . . . .	29
3.16	Single via structure with three dielectric layers . . . . .	30
3.17	S-parameters of single via structure with three dielectric layers . . . . .	30
4.1	Cut-through view of a multilayer structure . . . . .	33
4.2	$S_{11}$ and $S_{12}$ of the through-hole via structure . . . . .	45
4.3	$S_{11}$ and $S_{12}$ of the through-hole via structure . . . . .	45
4.4	Top view of a three-layered interconnect with coupled sig- nal traces . . . . .	46
4.5	S-parameters of the three-layered interconnect with cou- pled signal traces by direct FEM and AMI . . . . .	47
4.6	S-parameters of the three-layered interconnect with cou- pled signal traces by direct FEM and FETI-DPEM . . . . .	47
4.7	Three-layered interconnect with stitching vias . . . . .	48
4.8	S-parameter of the three-layered interconnect with stitch- ing vias (separation of 120 mil) . . . . .	50

4.9	S-parameter of the three-layered interconnect with stitching vias (separation of 240 mil)	51
4.10	Three-layered interconnect with stitching vias	52
4.11	S-parameter of the three-layered interconnect without stitching vias	54

# CHAPTER 1

## INTRODUCTION

A digital integrated circuit (IC) consists of two parts: transistors and interconnects. With the increased integration and design complexities and the continuous demand for higher operating frequency and sharper rising time in the very large-scale integration (VLSI) technology, the interconnect effects are no longer negligible [1–3]. From a microscopic point of view, the digital signal can be considered as electromagnetic waves propagating among transistors through interconnects. When the gate delay that transistors take to process the signals keeps being reduced, the interconnect delay that the signal spends on traveling along the interconnects tends to dominate the overall performance of an integrated circuit. Interconnects are also believed to be responsible for many of the signal integrity issues and electromagnetic interference problems which are the potential causes of malfunctionings of the assembled circuits and the failures of the distorted signals in meeting with design requirements. Due to the long period and high expense in the practical design cycles, it is hence extremely necessary for the designers to be aware of the interconnect effects through modeling and simulation techniques in the very early design stages.

Interconnects fall into four categories [4]: on-chip interconnects provide the on-chip metallization and IC packaging; chip-to-chip interconnects connect pins or pads among chips and/or with other components, and the most common chip-to-chip interconnect is printed circuit boards (PCBs); module-to-module interconnects, as the highest level interconnects inside a digital system, provide connections among subsystem modules, and one of the common examples on the module-to-module interconnects is the backplane or motherboard; system-to-system interconnects are responsible for sharing information at system level and over long distances, such as coaxial cables and optical fibers. Among all levels of the aforementioned interconnects, multi-layer interconnects, targeting higher packaging density, shorter signal delay,

and smaller chip/board dimension, become the imperative trend in the design of high-speed systems. However, it is a great challenge to efficiently and accurately model the high-speed interconnects in a multilayer structure. This challenge is attributed to the large problem size, the three-dimensional geometrical complexities, nonuniform material properties in the multilayer structure, and high aspect ratios of traces and vias dimensions with respect to the chip/board dimensions [5].

Current approaches of modeling interconnects can be categorized as circuit models and full-wave models. The circuit models utilizing the circuit parameters extracted through quasi-static assumptions are generally computationally efficient. However, the circuit models are accurate only within a certain range of operation frequency beyond which the quasi-static assumption is no longer valid. In that case, in order to retain the accuracy in the interconnect modeling we have to consider the fields components in all the directions as in the full-wave models. Generally, the full-wave approaches for characterizing multilayer interconnects include the finite element method [6], [7], the finite difference method [8], [9], and the moment method [10], [11]. Compared with the circuit models based on the circuit parameter extraction, the full-wave models can be very computational intensive primarily due to the spatial discretization.

In this work, we choose the finite element method as the foundation for the full-wave analysis of multilayer interconnects. Owing to the capability of dealing with arbitrary geometries, the finite element method has earned its popularity in handling complicated circuit structures. In order to enhance the efficiency of the full-wave analysis, two major algorithms have been investigated and incorporated into the finite element analysis, namely, the solution space projection [12] and the domain decomposition schemes [13], [14]. Generally, broadband information is mandatory for the circuit analysis and a frequency sweep needs to be performed. In other words, the linear system of a large dimension resulting from the volumetric discretization has to be factorized and solved repeatedly for many frequency samples. It can be imagined that such a frequency sweep will make the full-wave analysis extremely computationally intensive and sometimes it becomes an impossible task to tackle. The fast frequency sweep, particularly the method of solution space projection [12] in this work, will enhance the efficiency of the full-wave analysis over a broadband. The details of the method of solution space pro-

jection will be provided in later chapters and it is worth mentioning that by employing the solution vectors at a few selected frequency samples and forming a reduced-order model to accurately represent the original problem, the frequency sweep can be extremely efficient.

Another approach available to enhance the efficiency of the full-wave analysis is domain decomposition. In practical application, a problem can be really large, and sometimes doing the mesh itself would be an impossible task, not to mention solving the problem. By applying domain decomposition, instead of tackling the entire problem as a whole, one can divide it into smaller pieces. The domain decomposition schemes also allow the possibility of parallel computing which will further enhance the efficiency. Two domain decomposition schemes are investigated in this work: one is the approximate modal interface (AMI) method [13], devised for the multilayer structure and utilizing modal field expansion to perform decomposition and recoupling among the layers; the other approach, named the finite element tearing and interconnecting method [14], can be considered as a two-way decomposition, not only by layers as AMI does but also within each individual layer. Therefore, the finite element tearing and interconnecting method is more flexible in terms of decomposing the computational domains.

This work is organized as follows: in Chapter 2 the full-wave analysis based on the finite element method is formulated to solve circuit problems. The applications of the absorbing boundary condition and the port boundary condition are also presented in Chapter 2. Chapter 3 elaborates on the method of solution space projection and validates the implementation with various numerical examples. Chapter 4 focuses on the two aforementioned domain decomposition schemes, namely, the approximate modal interface method and the finite element tearing and interconnecting method. In Chapter 4, the domain decomposition schemes and the fast frequency sweep technique are combined in a mutually beneficial manner for a further enhancement of the full-wave analysis. Numerical examples are also provided in Chapter 4 to validate the implementation and demonstrate the efficiency for the domain decomposition schemes. The entire work concludes in Chapter 5.

# CHAPTER 2

## THREE-DIMENSIONAL FINITE ELEMENT FORMULATION

### 2.1 The Boundary Value Problem

The finite element method is applied to solve the vector wave equation

$$\nabla \times \left( \frac{1}{\mu_r} \nabla \times \mathbf{E} \right) - k_0^2 \epsilon_r \mathbf{E} = -jk_0 Z_0 \mathbf{J} \quad (2.1)$$

where  $\epsilon_r$  and  $\mu_r$  are the relative permittivity and permeability, respectively;  $Z_0$  is the intrinsic impedance of free space;  $\mathbf{J}$  is the density of the excitation current source; and  $k_0$  is the frequency at which the source is excited.

In order to solve for  $\mathbf{E}$ , which satisfies the vector wave equation in Equation (2.1), one has to apply boundary conditions. The boundary conditions frequently used in the electromagnetic simulations include the homogeneous Dirichlet boundary condition

$$\hat{n} \times \mathbf{E} = 0 \quad (2.2)$$

and the boundary condition of the third kind

$$\frac{1}{\mu_r} \hat{n} \times (\nabla \times \mathbf{E}) + \gamma_e \hat{n} \times (\hat{n} \times \mathbf{E}) = \mathbf{U} \quad (2.3)$$

where  $\hat{n}$  is a normal unit vector to the boundary surface and points outward from the surface;  $\gamma_e$  is a constant; and  $\mathbf{U}$  represents the source that exists on the boundary surface.

When  $\gamma_e$  and  $\mathbf{U}$  are both zero, the boundary condition of the third kind reduces to the Neumann boundary condition as

$$\hat{n} \times (\nabla \times \mathbf{E}) = 0. \quad (2.4)$$

The boundary condition of the third kind also includes the absorbing boundary condition (ABC) and the port boundary condition (PBC). The Dirichlet boundary condition in Equation (2.2) represents the perfect electric conductors (PECs) and are commonly used to model conductors and side walls in the circuit structures. The absorbing boundary conditions are typically employed to truncate the computational domain into a finite one. The port boundary conditions are attached on port surfaces as excitations to the circuit structures. It is worth mentioning that when the ports are not excited they function as the absorbing boundaries to truncate the computational domain. The details of the absorbing boundary condition and the port boundary condition are provided in the later sections.

## 2.2 Absorbing Boundary Condition

The finite element analysis can only be applied to a finite computational domain whereas in most circuit problems one deals with unbounded or open structures. Therefore, some artificial boundary conditions are required to truncate an infinite computational domain. The artificial boundary conditions should at the same time be able to simulate the extension of the computational domain into infinity. One such boundary condition is absorbing boundary condition. It establishes relations among local unknowns attached on the side walls of the circuit structures and lying on the outer surface of the computational domain. Because of the localized relation introduced by absorbing boundary condition, the sparsity of the finite element system matrices is preserved.

### 2.2.1 Absorbing Boundary Condition

The simplest absorbing boundary condition is the first-order condition, which is adopted here. Neglecting terms of order  $\frac{1}{r^3}$  and higher, the scattered field  $\mathbf{E}^{\text{sca}}$  in a scattering analysis can be written as

$$\frac{1}{\mu_r} \hat{n} \times (\nabla \times \mathbf{E}^{\text{sca}}) + jk_0 \sqrt{\frac{\epsilon_r}{\mu_r}} \hat{n} \times (\hat{n} \times \mathbf{E}^{\text{sca}}) = 0. \quad (2.5)$$

Note that the incident field  $\mathbf{E}^{\text{inc}}$ , the scattered field  $\mathbf{E}^{\text{sca}}$ , and the total field  $\mathbf{E}$  have the relation

$$\mathbf{E} = \mathbf{E}^{\text{inc}} + \mathbf{E}^{\text{sca}}. \quad (2.6)$$

With Equation (2.6), Equation (2.5) can be re-written in terms of the total field  $\mathbf{E}$  as

$$\frac{1}{\mu_r} \hat{n} \times (\nabla \times \mathbf{E}) + jk_0 \sqrt{\frac{\epsilon_r}{\mu_r}} \hat{n} \times (\hat{n} \times \mathbf{E}) = \mathbf{U}^{\text{inc}} \quad (2.7)$$

where  $\mathbf{U}^{\text{inc}}$  is defined by

$$\mathbf{U}^{\text{inc}} = \frac{1}{\mu_r} \hat{n} \times (\nabla \times \mathbf{E}^{\text{inc}}) + jk_0 \sqrt{\frac{\epsilon_r}{\mu_r}} \hat{n} \times (\hat{n} \times \mathbf{E}^{\text{inc}}). \quad (2.8)$$

As the circuit excitation is locally constructed and there is no incident field from side walls,  $\mathbf{U}^{\text{inc}}$  is zero. The absorbing boundary condition becomes

$$\frac{1}{\mu_r} \hat{n} \times (\nabla \times \mathbf{E}) + jk_0 \sqrt{\frac{\epsilon_r}{\mu_r}} \hat{n} \times (\hat{n} \times \mathbf{E}) = 0. \quad (2.9)$$

### 2.2.2 Finite Element Formulation

Applying the Galerkin method to Equation (2.1), the residual  $R$  is

$$\begin{aligned} R = \int_V \mathbf{W} \cdot \left[ \nabla \times \left( \frac{1}{\mu_r} \nabla \times \mathbf{E} \right) \right] dv - k_0^2 \int_V \epsilon_r \mathbf{W} \cdot \mathbf{E} dv \\ + jk_0 Z_0 \int_V \mathbf{W} \cdot \mathbf{J} dv, \end{aligned} \quad (2.10)$$

where  $\mathbf{W}$  is the testing function and  $V$  denotes the volume of the computational domain.

With the vector identity

$$\nabla \cdot (\mathbf{A} \times \mathbf{B}) = \mathbf{B} \cdot (\nabla \times \mathbf{A}) - \mathbf{A} \cdot (\nabla \times \mathbf{B}), \quad (2.11)$$

the first term on the right side of Equation (2.10) becomes

$$\begin{aligned} \int_V \mathbf{W} \cdot \left[ \nabla \times \left( \frac{1}{\mu_r} \nabla \times \mathbf{E} \right) \right] dv = \int_V \nabla \cdot \left[ \left( \frac{1}{\mu_r} \nabla \times \mathbf{E} \right) \times \mathbf{W} \right] dv \\ + \int_V \frac{1}{\mu_r} (\nabla \times \mathbf{W}) \cdot (\nabla \times \mathbf{E}) dv. \end{aligned} \quad (2.12)$$

With the divergence theorem, the first term on the right-hand side of Equation (2.12) can be written as

$$\begin{aligned} \int_V \nabla \cdot \left[ \left( \frac{1}{\mu_r} \nabla \times \mathbf{E} \right) \times \mathbf{W} \right] dv &= \int_S \left[ \left( \frac{1}{\mu_r} \nabla \times \mathbf{E} \right) \times \mathbf{W} \right] \cdot \hat{n} ds \\ &= \int_S \mathbf{W} \cdot \left[ \hat{n} \times \left( \frac{1}{\mu_r} \nabla \times \mathbf{E} \right) \right] ds. \end{aligned} \quad (2.13)$$

With the above derivations, the residual in Equation (2.10) can be written as

$$\begin{aligned} R &= \int_V \frac{1}{\mu_r} (\nabla \times \mathbf{W}) \cdot (\nabla \times \mathbf{E}) dv \\ &\quad - k_0^2 \int_V \epsilon_r \mathbf{W} \cdot \mathbf{E} dv \\ &\quad + \int_S \mathbf{W} \cdot \left[ \hat{n} \times \left( \frac{1}{\mu_r} \nabla \times \mathbf{E} \right) \right] ds \\ &\quad + jk_0 Z_0 \int_V \mathbf{W} \cdot \mathbf{J} dv, \end{aligned} \quad (2.14)$$

where  $S$  denotes the surface boundary enclosing the volume. If there exists an absorbing boundary condition, one can further reduce Equation (2.14). On the absorbing boundary  $S_{abc}$ , the surface integral becomes

$$\int_S \mathbf{W} \cdot \left[ \hat{n} \times \left( \frac{1}{\mu_r} \nabla \times \mathbf{E} \right) \right] ds = jk_0 \int_{S_{abc}} \sqrt{\frac{\epsilon_r}{\mu_r}} (\hat{n} \times \mathbf{W}) \cdot (\hat{n} \times \mathbf{E}) ds. \quad (2.15)$$

The residual in Equation (2.10) can be finalized as

$$\begin{aligned} R &= \int_V \frac{1}{\mu_r} (\nabla \times \mathbf{W}) \cdot (\nabla \times \mathbf{E}) dv \\ &\quad - k_0^2 \int_V \epsilon_r \mathbf{W} \cdot \mathbf{E} dv \\ &\quad + jk_0 \int_{S_{abc}} \sqrt{\frac{\epsilon_r}{\mu_r}} (\hat{n} \times \mathbf{W}) \cdot (\hat{n} \times \mathbf{E}) ds \\ &\quad + jk_0 Z_0 \int_V \mathbf{W} \cdot \mathbf{J} dv. \end{aligned} \quad (2.16)$$

Let the residual be zero and assemble all the elemental matrices, we will

arrive at Equation (2.17) the matrix equation

$$(\mathbf{K}_0 - k_0 \mathbf{K}_1 - k_0^2 \mathbf{K}_2) \mathbf{x} = \mathbf{K} \mathbf{x} = \mathbf{b} \quad (2.17)$$

where the elemental matrices are defined as

$$\mathbf{K}_0^e = \int_{V^e} \frac{1}{\mu_r^e} (\nabla \times \mathbf{W}^e) \cdot (\nabla \times \mathbf{W}^e) dv \quad (2.18)$$

$$\mathbf{K}_1^e = -j \int_{S_{abc}^e} \sqrt{\frac{\epsilon_r^e}{\mu_r^e}} (\hat{n} \times \mathbf{W}^e) \cdot (\hat{n} \times \mathbf{W}^e) ds \quad (2.19)$$

$$\mathbf{K}_2^e = \int_{V^e} \epsilon_r^e \mathbf{W}^e \cdot \mathbf{W}^e dv \quad (2.20)$$

$$\mathbf{b}^e = -jk_0 Z_0 \int_{V^e} \mathbf{W}^e \cdot \mathbf{J}^e dv. \quad (2.21)$$

## 2.3 Wave Port

The full-wave analysis here requires waveguide port boundary conditions attached to the port surfaces to launch an incident wave into the circuit structures and at the same time absorb the reflected wave. Absorbing boundary condition based on the modal expansion has been proposed for such kind of port boundary. As in [15] the modal expansion on the port surface has been successfully incorporated into the finite element analysis.

### 2.3.1 Port Boundary Condition

Before deriving the port boundary condition, let us derive the relation:

$$\begin{aligned} \kappa_m &= \int_{\Gamma} \vec{\mathbf{h}}_{tm} \times \vec{\mathbf{e}}_{tm} \cdot \hat{n} d\Gamma \\ &= \frac{j}{\omega \mu} \int_{\Gamma} (\gamma_m \vec{\mathbf{e}}_{tm} \cdot \vec{\mathbf{e}}_{tm} + \vec{\mathbf{e}}_{tm} \cdot \nabla_t e_{zm}) d\Gamma \end{aligned} \quad (2.22)$$

where  $\kappa_m$  is a constant;  $\vec{\mathbf{h}}_{tm}$  and  $\vec{\mathbf{e}}_{tm}$  are the transverse components of the modal magnetic and electric fields on a port surface, respectively;  $\gamma_m$  is the propagation constant; and  $\hat{z}$  defines a local unit vector that points inward to the port such that  $\hat{z} = -\hat{n}$  where  $\hat{n}$  is the unit normal vector on a port

surface.

Starting with Maxwell's equations and applying the following operations

$$\begin{aligned}\nabla &= \nabla_t + \hat{z} \frac{\alpha}{\alpha z} \\ \mathbf{E}_m &= \vec{\mathbf{e}}_{tm} - \hat{z} e_{zm} \\ \mathbf{H}_m &= -\vec{\mathbf{h}}_{tm} + \hat{z} h_{zm},\end{aligned}\tag{2.23}$$

we have

$$\begin{aligned}\nabla \times \mathbf{E}_m &= (\nabla_t + \hat{z} \frac{\alpha}{\alpha z}) \times (\vec{\mathbf{e}}_{tm} - \hat{z} e_{zm}) \\ &= \nabla_t \times \vec{\mathbf{e}}_{tm}|_{\hat{z}} - \nabla_t \times (\hat{z} e_{zm})|_{\hat{z}^\perp} + \gamma_m \hat{z} \times \vec{\mathbf{e}}_{tm}|_{\hat{z}^\perp},\end{aligned}\tag{2.24}$$

where the subscript  $\hat{z}^\perp$  denotes the direction that is perpendicular to  $\hat{z}$ . Therefore,

$$\vec{\mathbf{h}}_{tm} = \frac{j}{\omega\mu} [-\nabla_t \times (\hat{z} e_{zm}) + \gamma_m \hat{z} \times \vec{\mathbf{e}}_{tm}].\tag{2.25}$$

Because

$$\begin{aligned}\nabla_t \times (\hat{z} e_{zm}) &= e_{zm} (\nabla_t \times \hat{z}) - \hat{z} \times \nabla_t e_{zm} \\ &= -\hat{z} \times \nabla_t e_{zm},\end{aligned}\tag{2.26}$$

we have

$$\vec{\mathbf{h}}_{tm} = \frac{j}{\omega\mu} \hat{z} \times (\nabla_t e_{zm} + \gamma_m \vec{\mathbf{e}}_{tm}).\tag{2.27}$$

Now, let us go back to the target equation

$$\begin{aligned}(\vec{\mathbf{h}}_{tm} \times \vec{\mathbf{e}}_{tm}) \cdot \hat{n} &= \frac{j}{\omega\mu} \{ [-\hat{n} \times (\nabla_t e_{zm} + \gamma_m \vec{\mathbf{e}}_{tm})] \times \vec{\mathbf{e}}_{tm} \} \cdot \hat{n} \\ &= -\frac{j}{\omega\mu} \vec{\mathbf{e}}_{tm} \cdot [\hat{n} \times \hat{n} \times (\nabla_t e_{zm} + \gamma_m \vec{\mathbf{e}}_{tm})] \\ &= \frac{j}{\omega\mu} (\vec{\mathbf{e}}_{tm} \cdot \nabla_t e_{zm} + \gamma_m \vec{\mathbf{e}}_{tm} \cdot \vec{\mathbf{e}}_{tm}).\end{aligned}\tag{2.28}$$

If the port is excited by the incident field  $\mathbf{E}^{\text{inc}}$  on the surface, there will be reflected field  $\mathbf{E}^{\text{sca}}$  that can be expressed as a linear combination of the modal fields. Thus the total field  $\mathbf{E}$  is in the form of

$$\mathbf{E} = \mathbf{E}^{\text{inc}} + \sum_{n=1}^{\infty} c_n (\vec{\mathbf{e}}_{tn} - \hat{z} e_{zn}) e^{\gamma_n z}.\tag{2.29}$$

Employing the orthogonality condition for the modal fields,

$$\int_{\Gamma} \vec{\mathbf{h}}_{tm} \times \vec{\mathbf{e}}_{tm} \cdot \hat{\mathbf{n}} d\Gamma = 0 \quad m \neq n, \quad (2.30)$$

we can solve for the modal coefficient  $c_m$  as

$$c_m = \frac{1}{\kappa_m} e^{-\gamma_m z} \int_{\Gamma} \vec{\mathbf{h}}_{tm} \times (\mathbf{E} - \mathbf{E}^{\text{inc}}) \cdot \hat{\mathbf{n}} d\Gamma, \quad (2.31)$$

where  $\kappa_m$  is defined in Equation (2.22).

Substituting the expression of modal coefficient  $c_m$  into Equation (2.29), taking the curl on both sides, and crossing it with  $\hat{\mathbf{n}}$ , we have

$$\hat{\mathbf{n}} \times \nabla \times \mathbf{E} + P(\mathbf{E}) = \mathbf{U}^{\text{wp}}, \quad (2.32)$$

where

$$P(\mathbf{E}) = \sum_{n=1}^{\infty} \frac{1}{j\omega\mu\kappa_n} (\gamma_n \vec{\mathbf{e}}_{tn} + \nabla e_{zn}) \int_{\Gamma} \mathbf{E} \cdot (\gamma_n \vec{\mathbf{e}}_{tn} + \nabla e_{zn}) d\Gamma \quad (2.33)$$

$$\mathbf{U}^{\text{wp}} = \hat{\mathbf{n}} \times \nabla \times \mathbf{E}^{\text{inc}} + P(\mathbf{E}^{\text{inc}}). \quad (2.34)$$

If we only have the excitation from the dominant mode, then

$$\mathbf{E}^{\text{inc}} = (\vec{\mathbf{e}}_{t1} + \hat{\mathbf{z}} e_{z1}) e^{-\gamma_1 z}. \quad (2.35)$$

The wave port excitation vector  $\mathbf{U}^{\text{wp}}$  is reduced to

$$\mathbf{U}^{\text{wp}} = -2(\gamma_1 \vec{\mathbf{e}}_{t1} + \nabla_t e_{z1}). \quad (2.36)$$

### 2.3.2 Finite Element Formulation

Let us get back to Equation (2.14). If there is no additional source other than the wave port excitation, the term associated with the current source  $\mathbf{J}$  in Equation (2.14) disappears. Substituting the term  $\left[ \frac{1}{\mu_r} \hat{\mathbf{n}} \times (\nabla \times \mathbf{E}) \right]$  by

the port boundary condition yields the new residual expression

$$\begin{aligned}
R = & \int_V \frac{1}{\mu_r} (\nabla \times \mathbf{W}) \cdot (\nabla \times \mathbf{E}) dv \\
& - k_0^2 \int_V \epsilon_r \mathbf{W} \cdot \mathbf{E} dv \\
& + j k_0 \int_{S_{\text{abc}}} \sqrt{\frac{\epsilon_r}{\mu_r}} (\hat{n} \times \mathbf{W}) \cdot (\hat{n} \times \mathbf{E}) ds \\
& - \sum_{n=1}^{N_{\text{port}}} \int_{S_{\text{pbc}}} \frac{1}{\mu_r} \mathbf{W} \cdot P_n(\mathbf{E}) ds \\
& + \sum_{n=1}^{N_{\text{port}}} \int_{S_{\text{pbc}}} \frac{1}{\mu_r} \mathbf{W} \cdot U_n^{\text{wp}} ds.
\end{aligned} \tag{2.37}$$

Let the residual be zero and assemble all the elemental matrices, we will arrive at the matrix equation similar to Equation (2.17)

$$\left[ \mathbf{K}_0 - k_0 \mathbf{K}_1 - k_0^2 \mathbf{K}_2 - \sum_{n=1}^{N_{\text{port}}} \mathbf{B}_n \right] \mathbf{x} = \mathbf{K} \mathbf{x} = \sum_{n=1}^{N_{\text{port}}} \mathbf{b}_n^{\text{wp}} \tag{2.38}$$

where

$$\begin{aligned}
\mathbf{B}_n &= \int_{S_{\text{pbc}}} \frac{1}{\mu_r} \mathbf{W} \cdot P_n(\mathbf{E}) ds \\
\mathbf{b}_n^{\text{wp}} &= - \int_{S_{\text{pbc}}} \frac{1}{\mu_r} \mathbf{W} \cdot U_n^{\text{wp}} ds.
\end{aligned} \tag{2.39}$$

## 2.4 Basis Functions

The finite element method is formulated via Galerkin's method where the weighting functions are chosen to be the same as the basis functions. It is believed that using the same set of functions as basis and weighting functions to enforce the zero weighted residual will usually lead to the most accurate solution.

Two types of basis functions are employed in this work, namely, nodal basis functions and edge basis functions. Due to the scalar nature of the nodal basis functions, they are usually used to approximate physical quantities of scalars, such as the electric potential in electrostatic problems and the axial component of modal electric field in the full-wave modal analysis on a

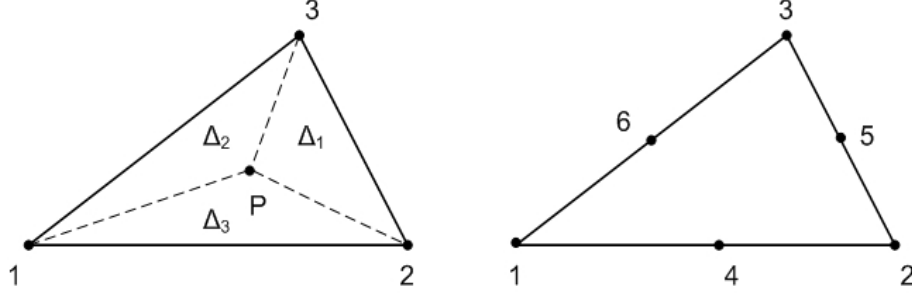


Figure 2.1: Nodal basis functions on triangular element

waveguide port. Edge basis functions or vector basis functions are used to approximate vector physical quantities, such as the transverse components of a modal electric field within triangular elements on a waveguide port surface, or the electric field in tetrahedral elements in a discretized volume.

#### 2.4.1 Simplex Coordinate

The two types of basis functions are constructed based on simplex coordinates. Consider the triangular element defined in Figure 2.1, where  $\Delta_i$  defines the area of the subtriangle formed by point  $P(x, y)$  and any two of the three vertices, for example,

$$\Delta_2 = \frac{1}{2} \begin{vmatrix} 1 & x & y \\ 1 & x_1^e & y_1^e \\ 1 & x_3^e & y_3^e \end{vmatrix}. \quad (2.40)$$

With these, we can define the area coordinate as  $L_1 = \frac{\Delta_1}{\Delta_e}$ ,  $L_2 = \frac{\Delta_2}{\Delta_e}$ ,  $L_3 = \frac{\Delta_3}{\Delta_e}$  where  $\Delta_e$  is the area of the entire triangular element.  $(L_1, L_2, L_3)$  are also recognized as simplex coordinates. The simplex coordinates  $(L_1, L_2, L_3)$  depend on the position of P only.

#### 2.4.2 Node Basis Functions

Linear nodal basis functions are defined on the three vertices of the triangle, in terms of simplex coordinates, and they can be written as

$$N_1 = L_1, \quad N_2 = L_2, \quad N_3 = L_3.$$

It is obvious from the definition that  $N_i$  becomes 1 at vertex  $i$  and 0 at the other two vertices.

Another set of nodal basis functions that have been widely used in finite element analysis is quadratic nodal basis functions. They provide one higher order approximation than the linear set, and only work on scalar quantities as well. In terms of simplex coordinates, with the numbering of the basis functions following the node numbers in Figure 2.1, the quadratic nodal basis functions can be expressed as follows:

$$\begin{aligned} N_1 &= (2L_1 - 1)L_1, & N_2 &= (2L_2 - 1)L_2, & N_3 &= (2L_3 - 1)L_3, \\ N_4 &= 4L_1L_2, & N_5 &= 4L_2L_3, & N_6 &= 4L_3L_1. \end{aligned}$$

Like linear nodal basis functions,  $N_i$  will reach 1 at node  $i$  and 0 at all other nodes. This property automatically ensures the requirement of continuity along the boundaries of adjacent triangular elements within the formulation of finite element analysis. To be specific, the scalar electric potential or the axial component of a modal electric field will remain the same or continuous across the boundaries of adjacent triangular elements upon the expansion by the nodal basis functions.

Since only first- and second-order nodal basis functions are listed here, the interested readers are referred to [16] for the unified derivations of nodal basis functions of arbitrary orders.

### 2.4.3 Edge Basis Functions

Edge basis or vector basis functions are employed to approximate vector field quantities. For example, we use edge basis functions to expand the transverse components of a modal electric field on a waveguide port surface. For the three-dimensional full-wave analysis, the edge basis functions are used to approximate the electric field on tetrahedral elements.

As we can see from Figure 2.2, the edge basis functions are defined along the edges of a triangular or a tetrahedral element, and hence the continuity across element boundaries is only enforced on the tangential components. This allows a discontinuity on the normal components. If we use node basis functions and assign the same value on the boundaries, we are actually en-

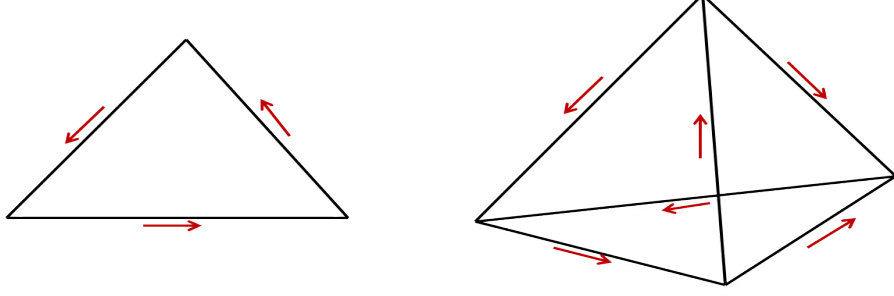


Figure 2.2: Edge basis functions on a triangular and tetrahedral element

forcing the continuity of both tangential and normal components of the field, which causes problems while dealing with dielectric interfaces. Even though there are remedies to either avoid or fix those problems, it is very inconvenient compared to the implementation with edge basis functions. Other than that, the edge basis functions satisfy the divergence condition in the source free region and eliminate the spurious modes in the modal analysis with nodal basis functions.

On a triangular element, the first-order edge basis functions are defined as

$$\begin{aligned}\mathbf{W}_1 &= (L_1 \nabla L_2 - L_2 \nabla L_1) e_1, \quad \mathbf{W}_2 = (L_3 \nabla L_1 - L_1 \nabla L_3) e_2, \\ \mathbf{W}_3 &= (L_3 \nabla L_1 - L_3 \nabla L_1) e_3,\end{aligned}$$

where  $L_i$  is the simplex coordinate, and  $e_i$  is the length of edge  $i$ . Note that the tangential component of each edge basis functions is constant along the edge it sits on and vanishes on all the other edges.

Similarly, the second-order edge basis functions on a triangular element are given by

$$\begin{aligned}\mathbf{W}_1 &= (3L_1 - 1)(L_1 \nabla L_2 - L_2 \nabla L_1) e_1, \quad \mathbf{W}_2 = (3L_2 - 1)(L_2 \nabla L_3 - L_1 \nabla L_3) e_1, \\ \mathbf{W}_3 &= (3L_2 - 1)(L_2 \nabla L_3 - L_3 \nabla L_2) e_2, \quad \mathbf{W}_4 = (3L_3 - 1)(L_2 \nabla L_3 - L_3 \nabla L_2) e_2, \\ \mathbf{W}_5 &= (3L_3 - 1)(L_3 \nabla L_1 - L_1 \nabla L_3) e_3, \quad \mathbf{W}_6 = (3L_1 - 1)(L_3 \nabla L_1 - L_1 \nabla L_3) e_3, \\ \mathbf{W}_7 &= \frac{9}{2} L_3 (L_1 \nabla L_2 - L_2 \nabla L_1) e_1, \quad \mathbf{W}_8 = \frac{9}{2} L_1 (L_2 \nabla L_3 - L_3 \nabla L_2) e_2.\end{aligned}$$

As shown in Figure 2.2, the first-order edge basis functions are defined on the edges of a tetrahedron. In terms of simplex coordinates, they are written

as

$$\begin{aligned}\mathbf{W}_1 &= (L_1 \nabla L_2 - L_2 \nabla L_1) e_{12}, \quad \mathbf{W}_2 = (L_2 \nabla L_3 - L_3 \nabla L_2) e_{23}, \\ \mathbf{W}_3 &= (L_3 \nabla L_1 - L_1 \nabla L_3) e_{31}, \quad \mathbf{W}_4 = (L_1 \nabla L_4 - L_4 \nabla L_1) e_{14}, \\ \mathbf{W}_5 &= (L_4 \nabla L_2 - L_2 \nabla L_4) e_{42}, \quad \mathbf{W}_6 = (L_3 \nabla L_4 - L_4 \nabla L_3) e_{34},\end{aligned}$$

where  $e_{ij}$  is the length of the edge from node  $i$  to node  $j$ .

The second-order edge basis functions consist of two parts, namely, the set of basis functions defined on edges and those on the faces. The second-order edge basis functions are given by

$$\begin{aligned}\mathbf{W}_1 &= (3L_1 - 1)(L_1 \nabla L_2 - L_2 \nabla L_1) e_{12}, & \mathbf{W}_2 &= (3L_2 - 1)(L_1 \nabla L_2 - L_2 \nabla L_1) e_{12} \\ \mathbf{W}_3 &= (3L_2 - 1)(L_2 \nabla L_3 - L_3 \nabla L_2) e_{23}, & \mathbf{W}_4 &= (3L_3 - 1)(L_2 \nabla L_3 - L_3 \nabla L_2) e_{23} \\ \mathbf{W}_5 &= (3L_3 - 1)(L_3 \nabla L_1 - L_1 \nabla L_3) e_{31}, & \mathbf{W}_6 &= (3L_1 - 1)(L_3 \nabla L_1 - L_1 \nabla L_3) e_{31} \\ \mathbf{W}_7 &= (3L_1 - 1)(L_1 \nabla L_4 - L_4 \nabla L_1) e_{14}, & \mathbf{W}_8 &= (3L_4 - 1)(L_1 \nabla L_4 - L_4 \nabla L_1) e_{14} \\ \mathbf{W}_9 &= (3L_4 - 1)(L_4 \nabla L_2 - L_2 \nabla L_4) e_{42}, & \mathbf{W}_{10} &= (3L_2 - 1)(L_4 \nabla L_2 - L_2 \nabla L_4) e_{42} \\ \mathbf{W}_{11} &= (3L_3 - 1)(L_3 \nabla L_4 - L_4 \nabla L_3) e_{34}, & \mathbf{W}_{12} &= (3L_4 - 1)(L_3 \nabla L_4 - L_4 \nabla L_3) e_{34} \\ \mathbf{W}_{13} &= \frac{9}{2} L_3 (L_1 \nabla L_2 - L_2 \nabla L_1) e_{12}, & \mathbf{W}_{14} &= \frac{9}{2} L_1 (L_2 \nabla L_3 - L_3 \nabla L_2) e_{23} \\ \mathbf{W}_{15} &= \frac{9}{2} L_4 (L_1 \nabla L_2 - L_2 \nabla L_1) e_{12}, & \mathbf{W}_{16} &= \frac{9}{2} L_2 (L_1 \nabla L_4 - L_4 \nabla L_1) e_{14} \\ \mathbf{W}_{17} &= \frac{9}{2} L_1 (L_3 \nabla L_4 - L_4 \nabla L_3) e_{34}, & \mathbf{W}_{18} &= \frac{9}{2} L_3 (L_1 \nabla L_4 - L_4 \nabla L_1) e_{14} \\ \mathbf{W}_{19} &= \frac{9}{2} L_2 (L_3 \nabla L_4 - L_4 \nabla L_3) e_{34}, & \mathbf{W}_{20} &= \frac{9}{2} L_4 (L_2 \nabla L_3 - L_3 \nabla L_2) e_{23}.\end{aligned}$$

# CHAPTER 3

## SOLUTION SPACE PROJECTION AND FAST FREQUENCY SWEEP

### 3.1 Solution Space Projection

A volumetric discretization in the finite element analysis leads to a large-dimensional system of equations. Even though the sparsity of the resulting linear system can be utilized by the ever-progressing direct or iterative sparse matrix solvers, it is still considered computational intensive especially when the broadband information is desired. Take the deterministic problem in Equation (2.38) for example. The space discretization results in the following matrix equation

$$\mathbf{K}(k)\mathbf{x}(k) = \mathbf{b}(k) \quad (3.1)$$

where  $k$  is the wave number. The matrix  $\mathbf{K}$ , the excitation vector  $\mathbf{b}$ , and the solution vector  $\mathbf{x}$  are all frequency-dependent. Therefore, a broadband analysis may require solving the system of equations at every single frequency sampling point, which is likely to result in a huge computation burden.

The solution space projection (SSP) method [12] to be introduced is devised for a fast and robust broadband finite element analysis. It is to construct a new model of the linear system in Equation (3.1) yet with a much smaller dimension; at the same time, the newly developed reduced-order model is capable of accurately describing the behaviors of the original linear system. With the reduced-order model, the broadband analysis requires solving a linear system of a much smaller dimension at the frequency samples, which tremendously reduces the computational burden.

The solution space projection possesses an adaptive multi-point nature. As the name *solution space projection* conveys, the original finite element model described by Equation (3.1) is projected onto a subspace spanned by a set of solution vectors. It is a set of frequency sampling points at which the

the original problem are solved and that reflects the nature of the multi-point scheme of SSP. The number and locations of the frequency samples are critical in constructing the reduced order model. An inadequate number of frequency samples will lead to an inaccurate prediction of the original problem while redundancy will downgrade the efficiency. In order to construct the reduced-order model in an accurate and efficient way, SSP bears an adaptive scheme such that the number of samples can be minimized.

### 3.2 Adaptive Multi-Point Scheme

As mentioned at the beginning of the chapter, if the solution over a given band is sought, the analysis must be repeated for many frequency sampling points in the range of interest, resulting in a high computational burden. Besides, due to the double integration, the port boundary information forms a dense matrix. It may lead to the degradation of the sparsity of the original  $\mathbf{K}$  matrix and an undesired large condition number of the final matrix. Further, for lossless medium in the circuit we usually expect a real system whereas the existence of wave ports will stuff complex entries into the system and force us to store the entire system in terms of complex numbers which actually doubles the storage. Fortunately, all those mentioned above can be avoided by the solution space projection method to be introduced in the following.

Assume that the dimension of the linear system in Equation (3.1) is  $N$ . The adaptive scheme starts with solving Equation (3.1) at the two ending frequency points  $k_{\text{start}}$  and  $k_{\text{end}}$ , and the obtained solution vectors are column-wise arranged to form  $\mathbf{X}$ . A set of basis vectors  $\mathbf{H}$  is then obtained through the orthonormalization of the solution vectors  $\mathbf{X}$ . The reduced-order model is formed by projecting the original linear system onto the subspace spanned by  $\mathbf{H}$  as

$$\mathbf{H}^H [\mathbf{K}(k)] \mathbf{H} \mathbf{y} = \mathbf{H}^H \mathbf{b}(k) \quad (3.2)$$

where the superscript  $H$  represents the transpose of the complex conjugate. It is worth mentioning that the recovery of the solution vector  $\mathbf{x}(k)$  of the original problem can simply be done by

$$\mathbf{x}(k) = \mathbf{H} \mathbf{y}(k). \quad (3.3)$$

The adaptive scheme requires the calculation of relative error  $\mathbf{r}$  at each step before expanding the set of solution vectors  $\mathbf{X}$  and consequently the set of basis vectors  $\mathbf{H}$ . The residual is calculated at the middle point  $k_{\text{mid}}$  of interval  $[k_{\text{start}} \ k_{\text{end}}]$ . At  $k_{\text{mid}}$ , we calculate the solution of the reduced order model  $\mathbf{y}(k_{\text{mid}})$  and project it back to the original problem denoted as  $\mathbf{H}\mathbf{y}(k_{\text{mid}})$ . The relative error is defined as

$$\mathbf{r} = \frac{|\mathbf{b}(k_{\text{mid}}) - [\mathbf{K}(k)]\mathbf{H}\mathbf{y}(k_{\text{mid}})|}{|\mathbf{b}(k_{\text{mid}})|}. \quad (3.4)$$

The adaptive process terminates if the relative error is below the specified tolerance, otherwise the original problem is solved at  $k_{\text{mid}}$  and the obtained solution vector is employed to expand the set of  $\mathbf{H}$ . After that, the relative errors at  $(k_{\text{min}} + k_{\text{mid}})/2$  and  $(k_{\text{mid}} + k_{\text{max}})/2$  are checked. The adaptive process will terminate only if both of the relative errors at  $(k_{\text{min}} + k_{\text{mid}})/2$  and  $(k_{\text{mid}} + k_{\text{max}})/2$  are below the preset tolerance. The solution vector at the frequency point of the larger relative error is used to expand the set of  $\mathbf{H}$ . The same procedure repeats until the relative errors at the middle points of all the existing intervals drop below the preset tolerance or the process hits the maximum number of iterations.

Suppose at the end the solutions at a total number of  $M$  sampling points are employed to construct the reduced-order model, when the frequency sweep is performed over the band of interest, a linear system of dimension  $M \times M$  instead of  $N \times N$  will be solved at each sampling point, where  $M$  is much smaller than  $N$ .

### 3.3 Numerical Examples

In this section, numerical examples will be provided as verifications of the three-dimensional FEM formulation with various boundary conditions and demonstrations of the robustness and efficiency of the method of solution space projection.

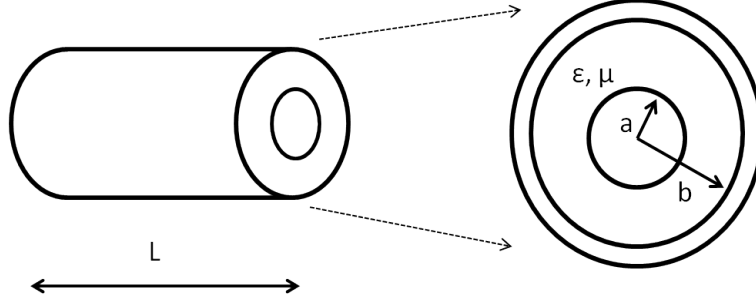


Figure 3.1: Coaxial transmission line

### 3.3.1 Conventional Waveguide Structures

Traditional metallic waveguide structures are common in microwave and RF devices. Even though the work targets at multilayer interconnects, examples of conventional waveguide structures are borrowed to verify the incorporation of solution space projection into the finite element analysis. Two waveguide examples, namely, coaxial cable and waveguide T-junction with discontinuity, are provided in the following.

#### 3.3.1.1 Coaxial Cable

Consider a lossy coaxial cable of 1 m length shown in Figure 3.1. The inner and outer radii of the coaxial cable are 0.4 mm and 1 mm, respectively. The relative permittivity of the dielectric between the two conducting walls is chosen to be  $\epsilon = 1 - 0.2j$ . S-parameters are calculated over the frequency range from 10 MHz to 1 GHz at 80 discrete sampling points. Different boundary conditions are applied at the two side surfaces in order to validate the implementation.

In Figure 3.2 and Figure 3.3, a PMC or PEC surface attached to the end of the coaxial port acts as open-circuit load or short-circuit load, respectively. The results obtained from full-wave analysis is compared to the analytical solutions, where the comparison verifies the correctness of the full-wave analysis implementation. However, it takes only five frequency points to build the reduced-order model, by which the solution vectors at all other sampling points are expanded. Therefore, instead of solving at every single frequency point out of 80, the solution space projection only employs five of them. It saves a tremendous amount of time and enables the fast frequency sweep.

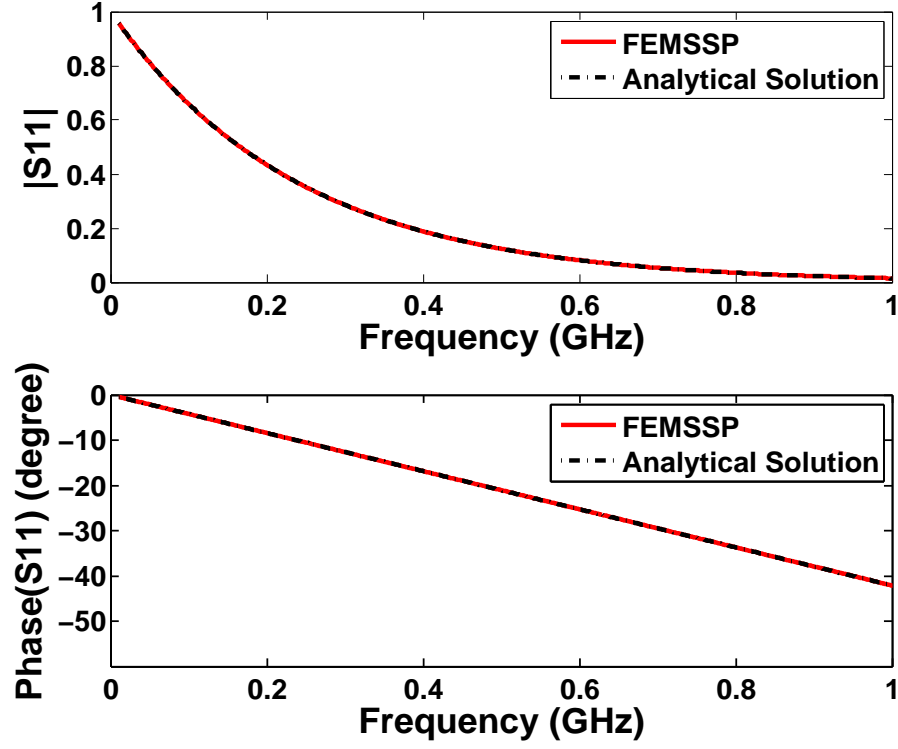


Figure 3.2: S-parameters of lossy coaxial cable with wave port and open-circuit load

Figure 3.4 and Figure 3.5 are taken as the validations of the implementations of an absorbing boundary condition (ABC) and a port boundary condition. As we know, ABC acts as transparent when wave penetrates on it, and it serves as a matched load for the coaxial cable. Therefore, we see no reflections at the incident end. As the frequency goes higher, it is observed that the portion of the transmitted wave reduces since the lossy transmission line consumes more power at higher frequencies.

### 3.3.1.2 Waveguide T-Junction

The second example is an H-plane waveguide T-junction with a metal block loaded inside. The detailed dimensional information can be found in Figure 3.6 and also in [17]. The frequency band of interest ranges over from 8 GHz to 12 GHz with 200 samples. With the method of solution space projection, the original problem is solved at five adaptively selected frequency samples with the predetermined tolerance of 0.001. The obtained results with solution space projection are compared with those in [15] and the two are identical

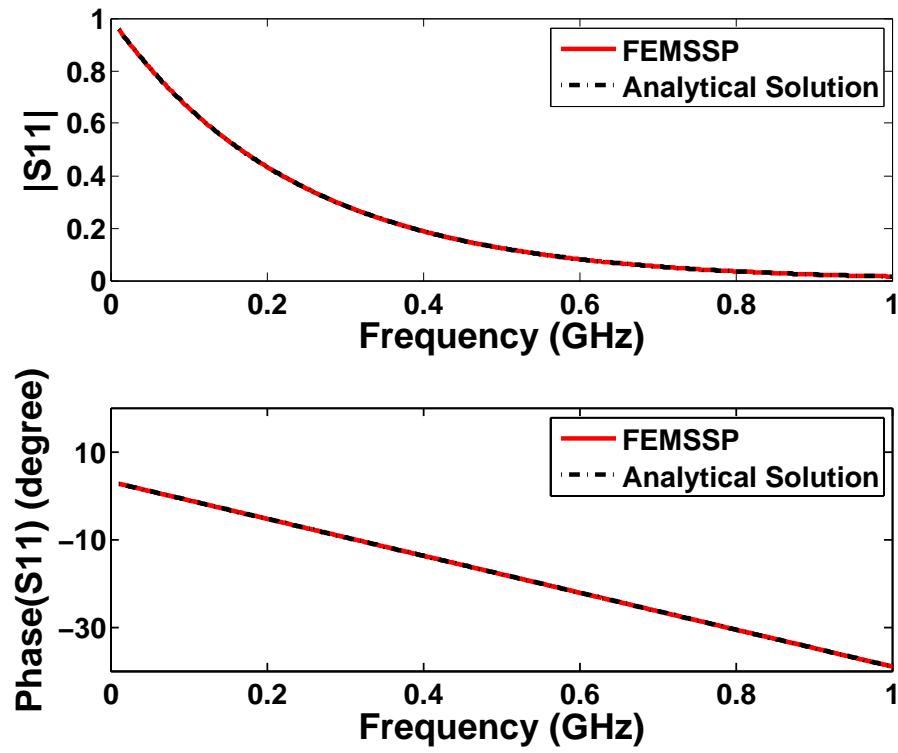


Figure 3.3: S-parameters of lossy coaxial cable with wave port and short-circuit load

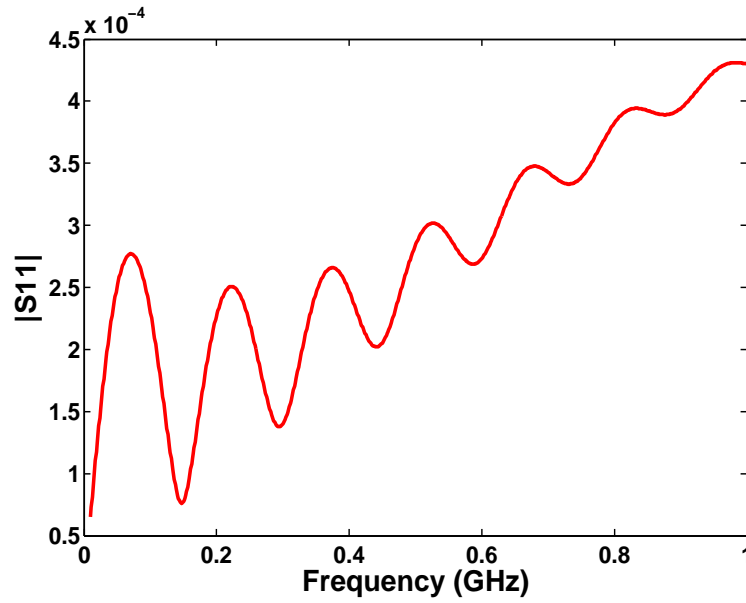


Figure 3.4: S-parameters of lossy coaxial cable with wave port and absorbing boundary condition

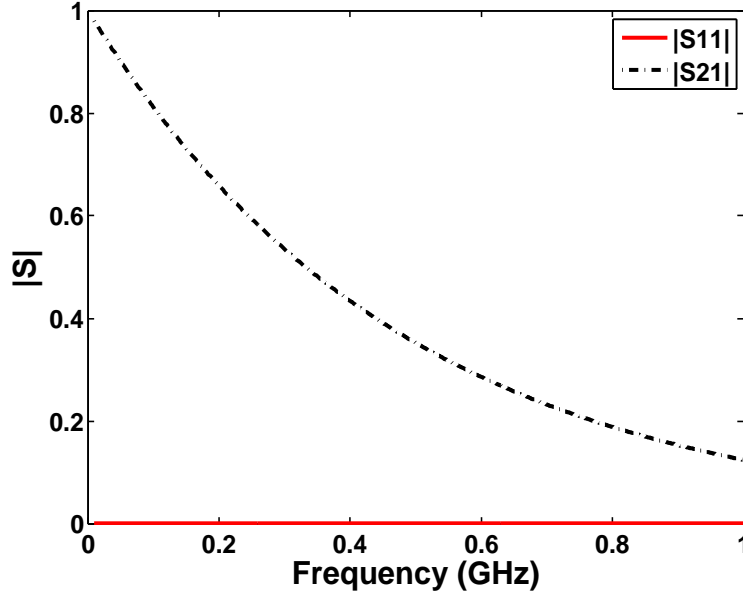


Figure 3.5: S-parameters of lossy coaxial cable with wave ports at both ends

as in Figure 3.7.

### 3.3.2 Planar Circuit Components

The bulky metallic waveguide structures are gradually replaced by the planar structures with the development of integrated circuit technology. Comparing to conventional waveguide structures, planar structures are compact and low cost. It also allows the possibility to integrate several planar components together with other active devices such as diodes and transistors, all of which are held on a single substrate, and the entire system can be mass-produced in a rather cost-effective manner by photolithography. In this section several examples of planar circuit components are provided. It is worth mentioning that the full-wave analysis of these planar structures are more challenging than for the conventional waveguide structures due to the existence of inhomogeneity and open structures.

#### 3.3.2.1 Microstrip Low-Pass Filter

In this example, we calculate the scattering parameters of a low-pass filter using the solution space projection method. As in Figure 3.8, the detailed

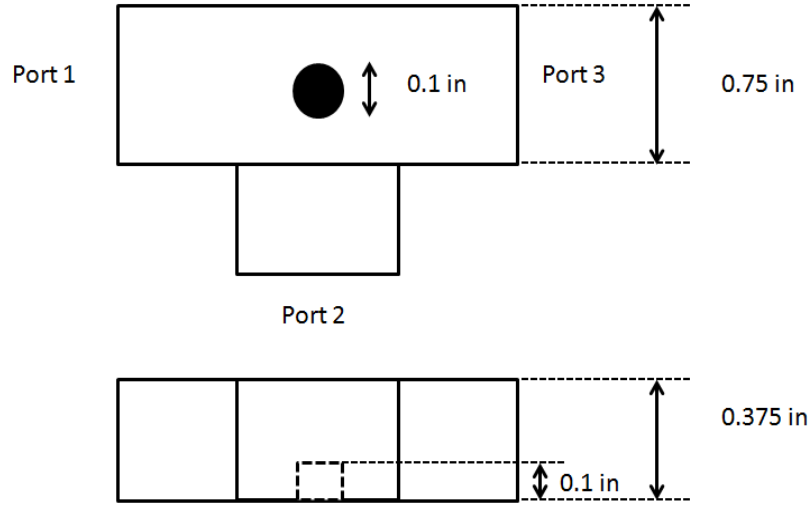


Figure 3.6: Top view and front view of a metal-loaded H-plane waveguide T-junction

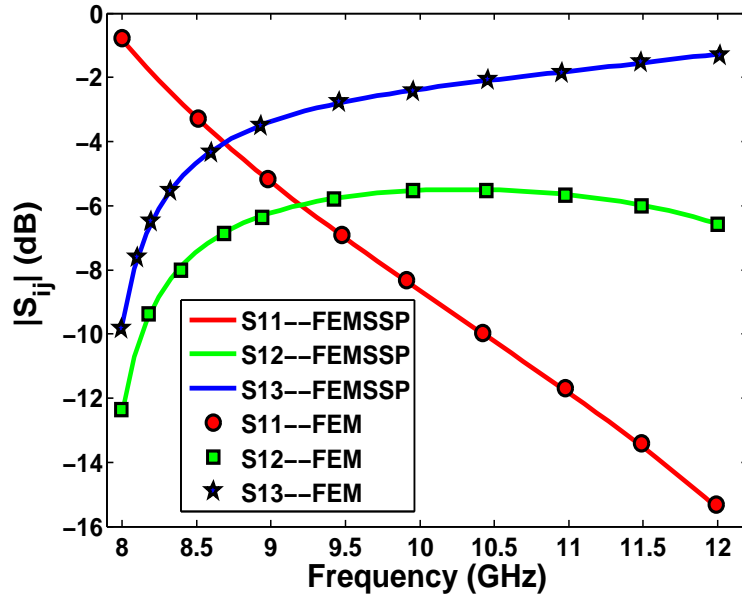


Figure 3.7: S-parameters of a metal-loaded H-plane waveguide T-junction

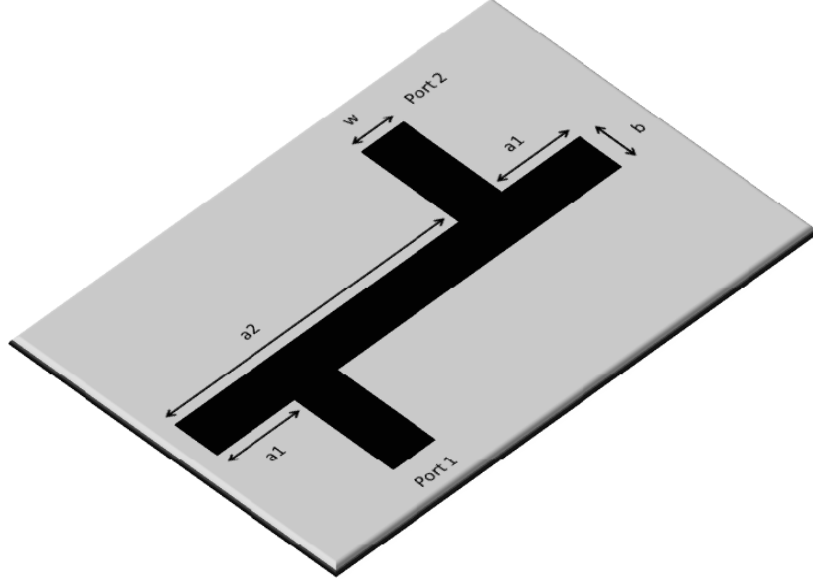


Figure 3.8: Microstrip low-pass filter

geometry information are  $w = 2.413$  mm,  $b = 2.54$  mm,  $a1 = 5.65$  mm,  $a2 = 12.257$  mm, the substrate height is 0.794 mm, and the relative permittivity of the substrate is  $\epsilon_r = 2.2$ . The desired frequency range is from 1 GHz to 20 GHz with 400 samples. The solution space projection is used with the tolerance for the adaptive procedure set to be 0.005. The reduced-order model is built with solutions at 11 adaptively selected frequency sampling points.

The results with both the FDTD method and the measurement are available in [18], with which a comparison is performed. Figures 3.9 and 3.10 show the results of comparison of insertion loss and return loss, respectively. The results with the solution space projection agree well with those from the FDTD method and measurement in the desired frequency range. It is worth mentioning that the measurement performed in [18] employed network analyzer and associated connectors that are rated only to 18 GHz, which explains the minor discrepancies occur at high frequencies.

### 3.3.2.2 Microstrip Branch Line Coupler

A microstrip branch coupler is shown in Figure 3.11. The four microstrip lines that branch out from the square have width  $w = 2.413$  mm, each of which is taken as a port. Also in Figure 3.11,  $a = 9.75$  mm and  $b = 3.96$

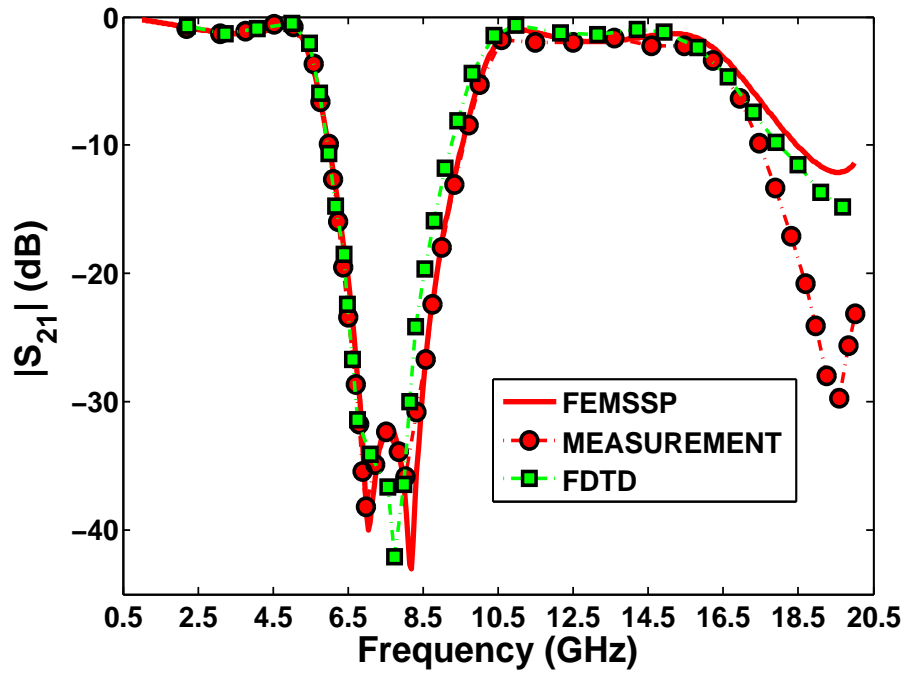


Figure 3.9: Insertion loss of a microstrip low-pass filter

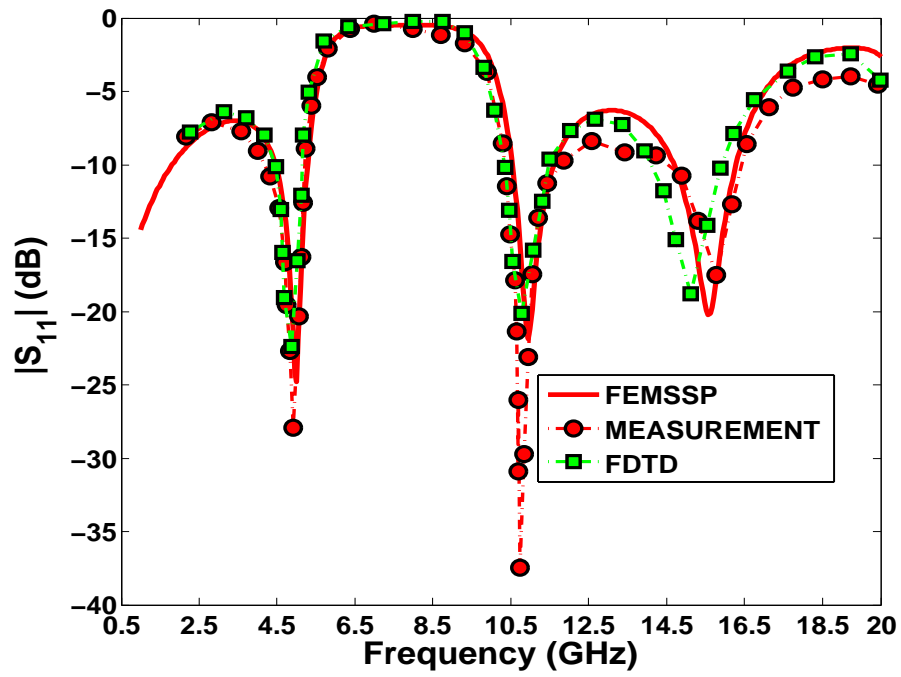


Figure 3.10: Return loss of a microstrip low-pass filter

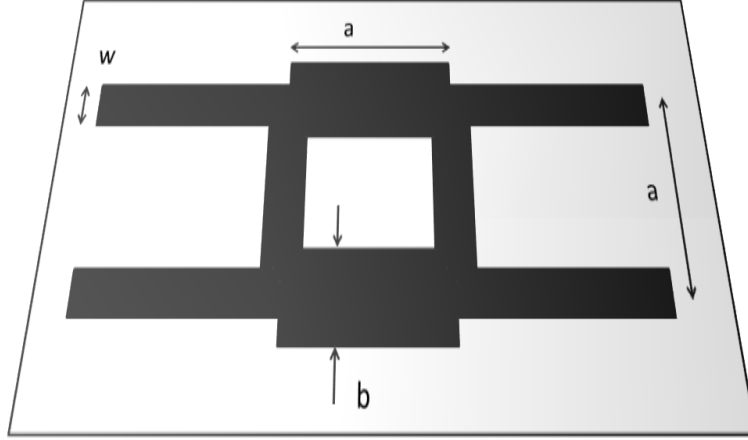


Figure 3.11: Microstrip branch line coupler

mm. The substrate has a height of 0.794 mm and permittivity  $\epsilon_r = 2.2$ .

To complete the broadband analysis from 100 MHz to 10 GHz, a number of 200 frequency samples are chosen over a linear scale. With the solution space projection method, only 9 out of 200 frequency samples are employed to build the reduced-order model. The predetermined tolerance of such an adaptive procedure is 0.002. The same structure has been examined with the FDTD method in [18]. It is shown in Figure 3.12 that the results here match well with those from the FDTD method.

### 3.3.3 Multilayer Board Interconnect

Interconnects find their existences on various levels such as printed circuit boards, packaging, and on-chip. Common interconnect structures include transitions, wire bonds, meander lines, and via structures. The trend of high-speed applications in the very large-scale integrated (VLSI) circuits has been highlighting the role of interconnects. As in a high-speed interconnect, the time that signals spend on traveling through the interconnect cannot be neglected. Generally, the interconnect is also responsible for signal integrity issues such as signal delays, distortions, reflections, and crosstalk. Therefore, it is essential for the designers to be aware of interconnect effects through modeling and simulation. However, the existing circuit simulators such as SPICE that depends on circuit parameter extractions cannot meet the requirement of accuracy especially as the frequency of operation goes higher. In this section, a few examples on the full-wave analysis of multi-

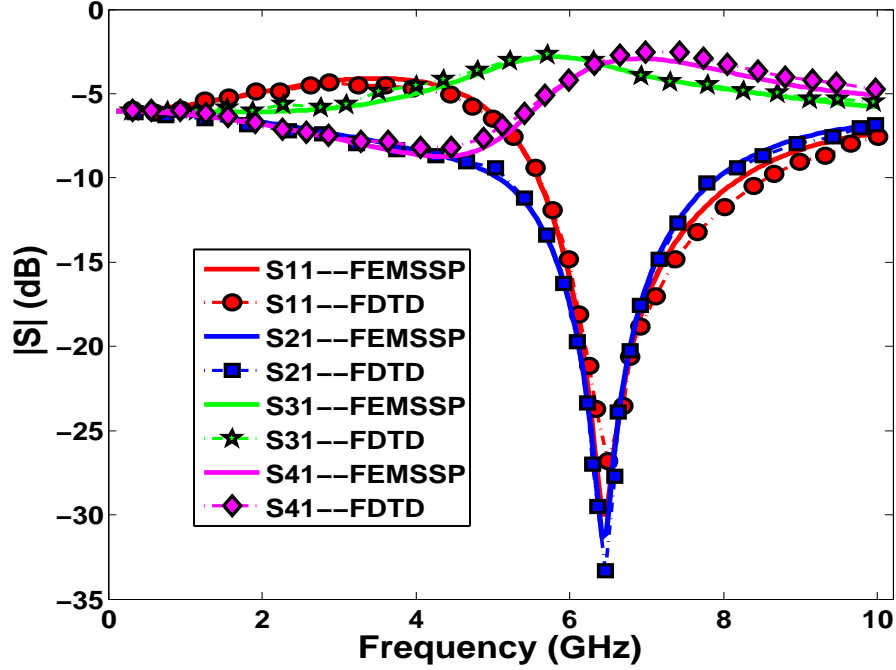


Figure 3.12: S-parameters of microstrip branch line coupler

layer interconnects are provided. Together with the method of solution space projection, the finite element analysis makes us closer to our goal of simulating interconnect structures as efficiently as possible while retaining high accuracy.

### 3.3.3.1 Single Via through Two Board Layers

The first via structure is a single via going through two dielectric layers which are separated by one ground plane as shown in Figure 3.13. The red shaded area in Figure 3.13(a) is considered as the ground plane that separates the dielectric layers. It is also shown that the clearance hole and the metal pad have the same diameter denoted as  $c$ . The via rod has a diameter denoted as  $d$ . The top and bottom dielectric layers share the same height  $h$ . In Figure 3.13(b), the microstrip with solid color is the strip attached onto the top of the via structure and the one enclosed by dash lines are the one attached onto the bottom, where  $\theta$  is the angle formed by the two microstrips.

Figure 3.14 shows the calculated S-parameters of the single via structure and the comparison with the result from measurement [19]. The angle between the top and bottom microstrips is  $\theta = 180^\circ$ . The diameter of the

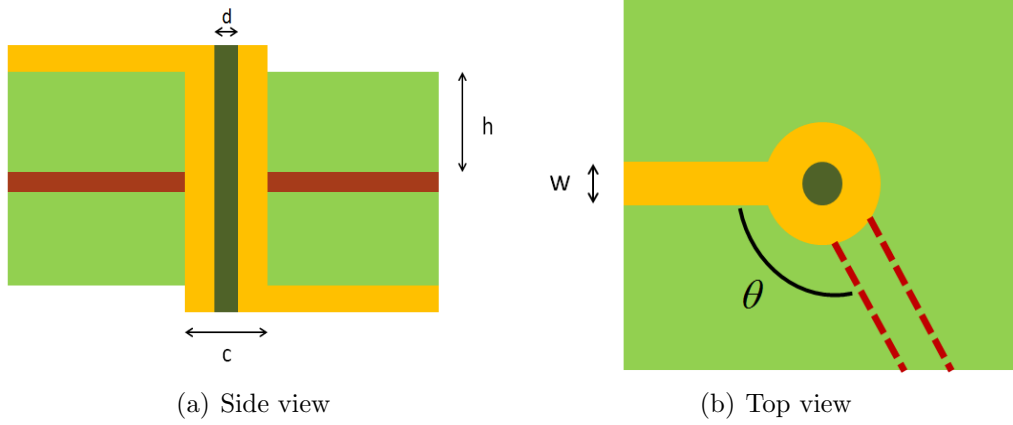


Figure 3.13: Single via structure with two dielectric layers

clearance hole (or via pad) is  $c = 3.9$  mm. The diameter of the via rod is  $d = 1.5$  mm. The width of the microstrip is  $w = 3.3$  mm. The substrate has a height  $h = 1.6$  mm and permittivity  $\epsilon_r = 3.4$ . The broadband analysis targets at the frequency range from 1 GHz to 25 GHz with 400 samples and only 14 of them are used to construct the reduced-order model.

Figure 3.15 is the calculated S-parameters of the same structure with  $\theta = 90^\circ$ . The obtained results with solution space projection are also compared with the measurement [19]. Everything remains the same except that the diameter of the via rod is changed to  $d = 0.7$  mm. The broadband analysis also considers 400 frequency sampling points from 1 GHz to 25 GHz and again only 14 of them are used to construct the reduced-order model.

### 3.3.3.2 Single Via through Three Board Layers

The last example of via structures is shown in Figure 3.16. The top and bottom microstrips are sitting on the same side. The detailed information of geometry is depicted in Figure 3.16. The frequency range of interest is from 100 MHz to 15 GHz with 200 samples. The reduced-order model is constructed with solutions at five frequency samples. Figure 3.17 shows the results and a comparison with the finite element analysis without the solution space projection. It can be seen that results from the two ways of simulation match pretty well.

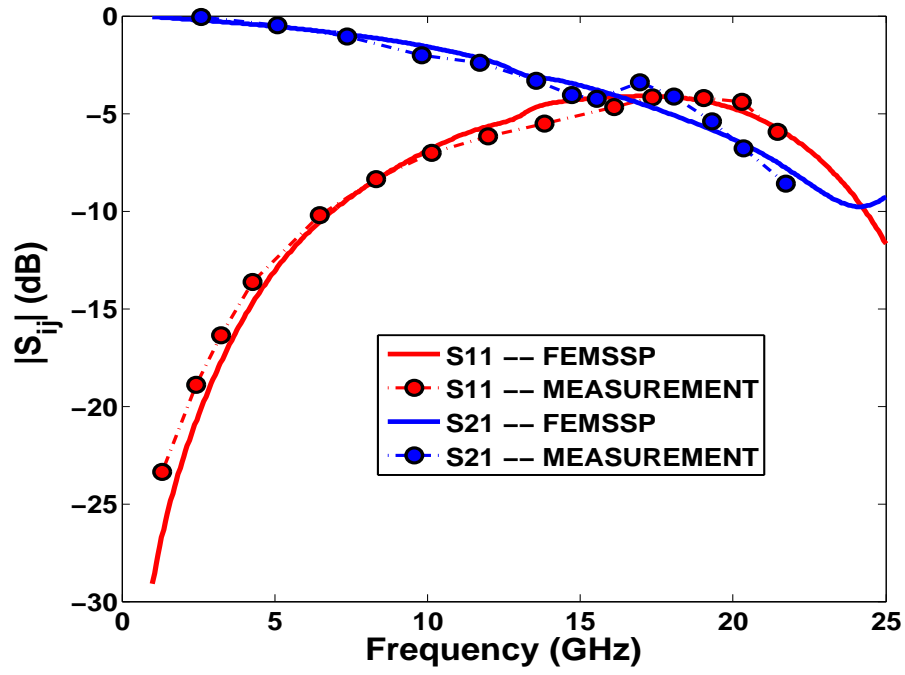


Figure 3.14: S-parameters of single via structure with  $\theta = 180^\circ$

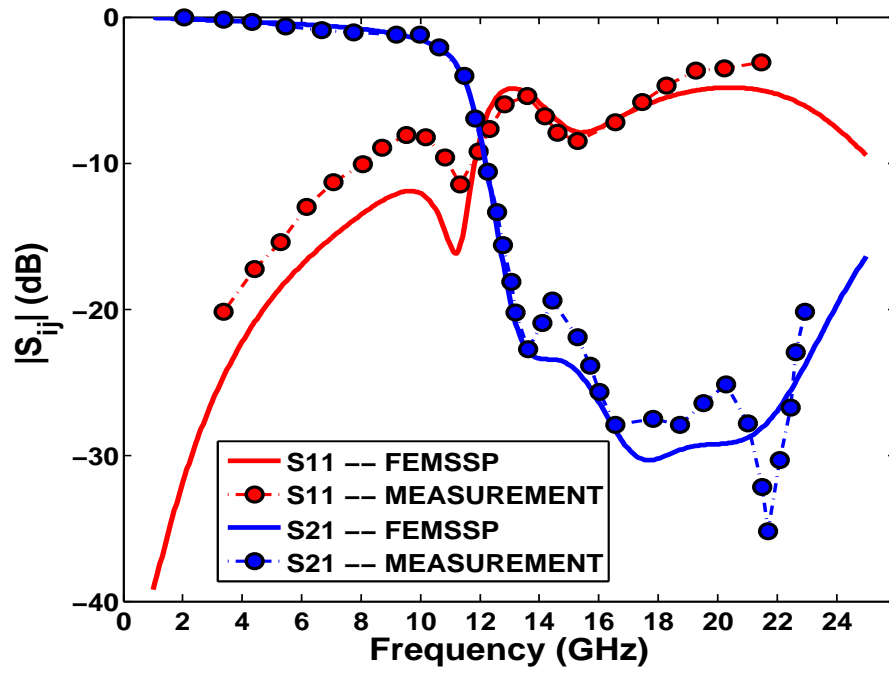


Figure 3.15: S-parameters of single via structure with  $\theta = 90^\circ$

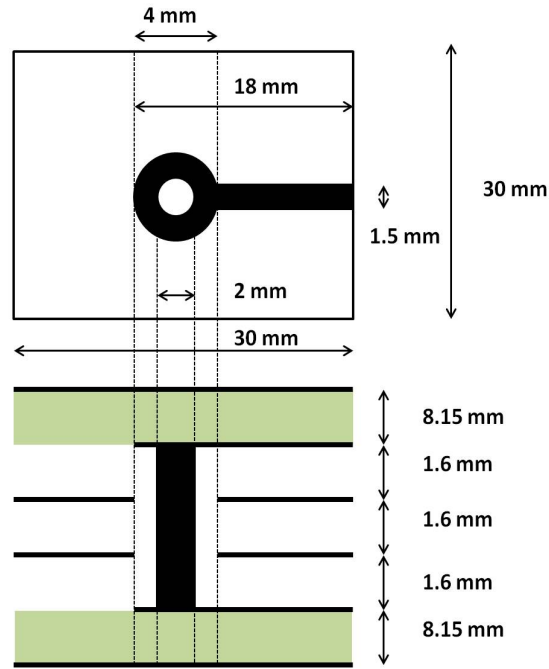


Figure 3.16: Single via structure with three dielectric layers

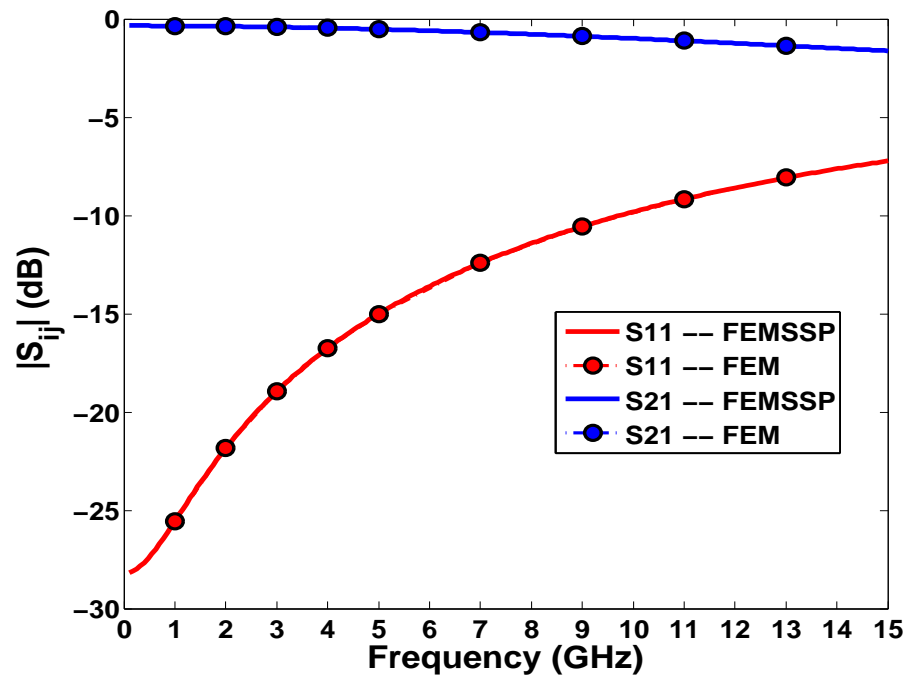


Figure 3.17: S-parameters of single via structure with three dielectric layers

# CHAPTER 4

## DOMAIN DECOMPOSITION OF THE MULTILAYER INTERCONNECTS

The modeling of the interconnects falls into two major categories, lumped models and distributed models. The selection between the lumped and distributed models depends on the operating frequency and the dimension of the interconnect itself. At relatively low frequencies, the interconnects can be modeled by lumped RC and RLC circuit models. As the frequency goes higher when the electrical length of the interconnect becomes significant comparing to the wavelength, the lumped circuit models are inadequate and transmission line models have to be adopted. Two major assumptions are made while assuming the transmission line models. One is the assumption on the transverse electromagnetic mode (TEM) where both electric field and magnetic field are perpendicular to the direction of propagation. This is valid only if the dimension of the line cross-section is much smaller than the wavelength. The other assumption is that the current is uniformly distributed over the cross-sectional area. However, as the frequency increases, the dimension of the cross-sectional area is comparable to or even larger than the wavelength; at the same time, the current distribution is no longer uniform over the cross-sectional area and the skin, edge, and proximity effects have to be taken into account. Besides, the inhomogeneity in most of the practical interconnect structures will also fail the TEM assumption by bringing in the E and H along the direction of propagation. All these aforementioned phenomena will degrade the accuracy of the transmission line models.

Even though people are attempting to modify the transmission line models by introducing distance-dependant and frequency-dependant R, L, C, G per unit length parameters to account for high-frequency effects, fields along the direction of the propagation cannot be neglected on a further increase of frequency. Consequently, the full-wave model, which takes into account all the spatial components of the fields, is inevitably the best alternative in modeling the interconnect structures. However, the full-wave analysis

can be considerably computational expensive. In this chapter, we proceed with the search for possibilities of fast and efficient full-wave analysis for the multilayer interconnects. We concentrate our work in this chapter on the methods of domain decomposition. The basic ideas of domain decomposition is to break the original problem into smaller ones and allow the possibility of parallel computing. Two schemes of domain decomposition are provided in this section, namely, the approximate modal interface (AMI) method [13] and the finite element tearing and interconnecting (FETI) [14] method. The approximate modal interface method is devised for the multilayer structures. It postulates the boundary conditions on the interfaces among layers and separates the original problem into smaller ones with each associated with one individual layer. The finite element tearing and interconnecting method is more general and flexible in terms of domain decomposition and it can be performed further within layers.

#### 4.1 Domain Decomposition by Layers: The Approximate Modal Interface Method

The approximate modal interface method [13] to be described here is devised for multilayer interconnects. In a multilayer interconnect structure, layers are separated by metallic planes. Assume perfect electric conductors (PECs) for the planes. The tangential component of electric field is zero everywhere on those PEC planes. If we can postulate the tangential components of electric fields at the apertures (via-holes), a complete set of boundary conditions for that particular layer can be obtained and the layer can thus be treated independently from the rest. If we apply this rationale to all the layers, information of every single layer can be extracted to form an independent problem. All these individual problems shall be re-coupled by the apertures shared by the neighboring layers.

Consider the multilayer structure shown in Figure 4.1. For simplicity, let us temporarily ignore the terms associated with the absorbing boundary

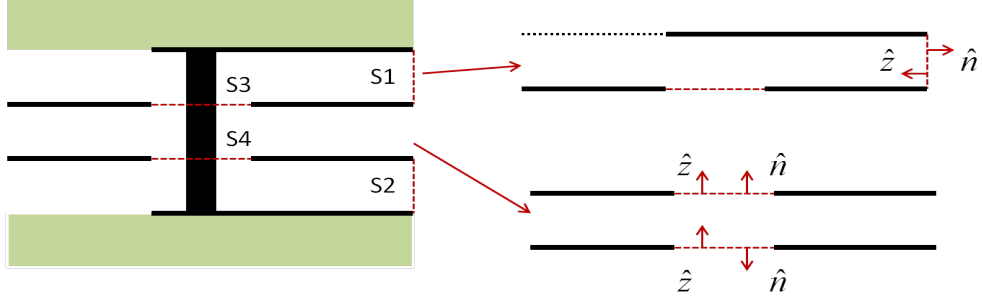


Figure 4.1: Cut-through view of a multilayer structure

condition. By Galerkin's method, the weighted residual can be expressed as

$$\begin{aligned}
 R = & \int_V \frac{1}{\mu_r} (\nabla \times \mathbf{W}) \cdot (\nabla \times \mathbf{E}) dv - k_0^2 \int_V \epsilon_r \mathbf{W} \cdot \mathbf{E} dv \\
 & + \int_S \mathbf{W} \cdot \left[ \hat{n} \times \left( \frac{1}{\mu_r} \nabla \times \mathbf{E} \right) \right] ds
 \end{aligned} \quad (4.1)$$

where  $S$  denotes the boundary surface. Since the absorbing boundary condition is temporarily ignored,  $S$  consists of wave port surfaces and the via-hole interfaces between two adjacent layers.

Assume that  $\mathbf{H}_i$  is the magnetic field at aperture  $S_i$ ,  $i = 1, 2, 3, 4$  in Figure 4.1, the electric field at the aperture can be obtained via Faraday's law as

$$\hat{n} \times \left( \frac{1}{\mu_r} \nabla \times \mathbf{E}_i \right) = -jk_0 Z_0 \hat{n} \times \mathbf{H}_i \quad (4.2)$$

where  $\hat{n}$  is the normal vector to  $S_i$  and points outward from  $S_i$  as shown in Figure 4.1. Treating Equation (4.2) as the boundary condition at the apertures and substituting it into Equation (4.1), one obtains

$$\begin{aligned}
 R = & \int_V \frac{1}{\mu_r} (\nabla \times \mathbf{W}) \cdot (\nabla \times \mathbf{E}) dv - k_0^2 \int_V \epsilon_r \mathbf{W} \cdot \mathbf{E} dv \\
 & - jk_0 Z_0 \sum_{i=1}^{N_s} \int_{S_i} \mathbf{W} \cdot (\hat{n} \times \mathbf{H}_i) ds.
 \end{aligned} \quad (4.3)$$

At aperture  $S_i$ , the magnetic field can be written as a linear combination of modal magnetic fields weighted by their corresponding modal coefficients

denoted as  $c_{i,k}$  ( $k$  stands for the  $k^{th}$  mode)

$$\mathbf{H}_i = \sum_{k=1}^{\text{Nmode}} c_{i,k} \mathbf{H}_{i,k}. \quad (4.4)$$

Again, by Faraday's law,

$$\mathbf{H}_{i,k} = \frac{c_{i,k}}{-jk_0 Z_0 \mu_r} \nabla \times (\vec{\mathbf{e}}_{ti,k} + \hat{z} e_{zi,k}) \quad (4.5)$$

where  $\vec{\mathbf{e}}_{ti}$  and  $\hat{z} e_{zi}$  represent the modal electric fields of the tangential direction and longitudinal direction, respectively. Substituting Equation (4.4) and Equation (4.5) into Equation (4.3), the third term of the weighted residual in Equation (4.3) becomes

$$\begin{aligned} & -jk_0 Z_0 \sum_{i=1}^{N_s} \int_{S_i} \mathbf{W} \cdot (\hat{n} \times \mathbf{H}_i) ds \\ &= \sum_{i=1}^{N_s} \sum_{k=1}^{\text{Nmode}} c_{i,k} \int_{S_i} \frac{1}{\mu_r} \mathbf{W} \cdot [\hat{n} \times \nabla \times (\vec{\mathbf{e}}_{ti,k} + \hat{z} e_{zi,k})] ds \\ &= \sum_{i=1}^{N_s} \sum_{k=1}^{\text{Nmode}} c_{i,k} \int_{S_i} \frac{1}{\mu_r} \mathbf{W} \cdot \left[ \hat{n} \times \left( \nabla_t + \hat{z} \frac{\alpha}{\alpha z} \right) \times (\vec{\mathbf{e}}_{ti,k} + \hat{z} e_{zi,k}) \right] ds \\ &= \sum_{i=1}^{N_s} \sum_{k=1}^{\text{Nmode}} c_{i,k} \int_{S_i} \frac{1}{\mu_r} \mathbf{W} \cdot \left[ \hat{n} \times (\nabla_t \times \vec{\mathbf{e}}_{ti,k} + \nabla_t \times (\hat{z} e_{zi,k}) + \hat{z} \times \left( \frac{\alpha}{\alpha z} \vec{\mathbf{e}}_{ti,k} \right)) \right] ds \\ &= \sum_{i=1}^{N_s} \sum_{k=1}^{\text{Nmode}} c_{i,k} \int_{S_i} \frac{1}{\mu_r} \mathbf{W} \cdot [\hat{n} \times (\nabla_t \times \vec{\mathbf{e}}_{ti,k} - \hat{z} \times \nabla_t e_{zi,k} - \hat{z} \times \gamma_{k,i} \vec{\mathbf{e}}_{ti,k})] ds \\ &= - \sum_{i=1}^{N_s} \sum_{k=1}^{\text{Nmode}} c_{i,k} \int_{S_i} \frac{1}{\mu_r} \mathbf{W} \cdot [\nabla_t e_{zi,k} + \gamma_{k,i} \vec{\mathbf{e}}_{ti,k}] ds. \end{aligned}$$

To conclude the preceding derivation,

$$-jk_0 Z_0 \sum_{i=1}^{N_s} \int_{S_i} \mathbf{W} \cdot (\hat{n} \times \mathbf{H}_i) ds = - \sum_{i=1}^{N_s} \sum_{k=1}^{\text{Nmode}} c_{i,k} \int_{S_i} \frac{1}{\mu_r} \mathbf{W} \cdot (\nabla_t e_{zi,k} + \gamma_{k,i} \vec{\mathbf{e}}_{ti,k}) ds. \quad (4.6)$$

Note that since  $\hat{n}$  and  $\hat{z}$  have opposite signs on all the apertures except those on the upper interface, a negative sign will appear in the right-hand side of Equation (4.6) except for the apertures on the upper interface. It is worth

mentioning that with Equation (4.6) all the formulations are now in terms of the electric field.

Enforcing the weighted residual to be zero and applying the finite element discretization, one obtains the system of equations

$$\begin{bmatrix} \mathbf{K}_{S_1 S_1} & 0 & \mathbf{K}_{S_1 V_1} \\ 0 & \mathbf{K}_{S_3 S_3} & \mathbf{K}_{S_3 V_1} \\ \mathbf{K}_{V_1 S_1} & \mathbf{K}_{V_1 S_3} & \mathbf{K}_{V_1 V_1} \end{bmatrix} \begin{bmatrix} \mathbf{E}_{S_1} \\ \mathbf{E}_{S_3} \\ \mathbf{E}_{V_1} \end{bmatrix} = \begin{bmatrix} \mathbf{b}_{S_1} \\ \mathbf{b}_{S_3} \\ 0 \end{bmatrix}, \quad (4.7)$$

where  $\mathbf{E}_{S_1}$ ,  $\mathbf{E}_{S_3}$ , and  $\mathbf{E}_{V_1}$  are the field coefficients of aperture  $S_1$ ,  $S_3$ , and volume  $V_1$ , respectively. The right-hand side excitation vector  $\mathbf{b}_{S_i}$  is given by

$$\mathbf{b}_{S_i} = \sum_{k=1}^{\text{Nmode}} c_{i,k} \int_{S_i} \frac{1}{\mu_r} \mathbf{W} \cdot (\nabla_t e_{zi,k} + \gamma_{k,i} \vec{e}_{ti,k}) ds. \quad (4.8)$$

Rewrite  $\mathbf{b}_{S_i}$  into the matrix form

$$\mathbf{b}_{S_i} = \begin{bmatrix} a_{i,1} & a_{i,2} & \dots & a_{i,k} & \dots & a_{i,N_{mode}} \end{bmatrix} \begin{bmatrix} c_{i,1} \\ c_{i,2} \\ \vdots \\ c_{i,k} \\ \vdots \\ c_{i,N_{mode}} \end{bmatrix} = \mathbf{A}_i \mathbf{c}_i. \quad (4.9)$$

With the matrix form of  $\mathbf{b}_{S_i}$ , the matrix form of Equation (4.7) can also be written as

$$\begin{bmatrix} \mathbf{E}_{S_1} \\ \mathbf{E}_{S_3} \\ \mathbf{E}_{V_1} \end{bmatrix} = \begin{bmatrix} \mathbf{K}_{S_1 S_1} & 0 & \mathbf{K}_{S_1 V_1} \\ 0 & \mathbf{K}_{S_3 S_3} & \mathbf{K}_{S_3 V_1} \\ \mathbf{K}_{V_1 S_1} & \mathbf{K}_{V_1 S_3} & \mathbf{K}_{V_1 V_1} \end{bmatrix}^{-1} \begin{bmatrix} \mathbf{A}_1 & 0 \\ 0 & \mathbf{A}_3 \\ 0 & 0 \end{bmatrix} \begin{bmatrix} \mathbf{c}_1 \\ \mathbf{c}_3 \end{bmatrix}. \quad (4.10)$$

Similarly, for the rest two layers, we have

$$\begin{bmatrix} \mathbf{E}_{S_3} \\ \mathbf{E}_{S_4} \\ \mathbf{E}_{V_2} \end{bmatrix} = \begin{bmatrix} \mathbf{K}_{S_3 S_3} & 0 & \mathbf{K}_{S_3 V_2} \\ 0 & \mathbf{K}_{S_4 S_4} & \mathbf{K}_{S_4 V_2} \\ \mathbf{K}_{V_2 S_3} & \mathbf{K}_{V_2 S_4} & \mathbf{K}_{V_2 V_4} \end{bmatrix}^{-1} \begin{bmatrix} -\mathbf{A}_3 & 0 \\ 0 & \mathbf{A}_4 \\ 0 & 0 \end{bmatrix} \begin{bmatrix} \mathbf{c}_3 \\ \mathbf{c}_4 \end{bmatrix} \quad (4.11)$$

$$\begin{bmatrix} \mathbf{E}_{S_2} \\ \mathbf{E}_{S_4} \\ \mathbf{E}_{V_3} \end{bmatrix} = \begin{bmatrix} \mathbf{K}_{S_2 S_2} & 0 & \mathbf{K}_{S_2 V_3} \\ 0 & \mathbf{K}_{S_4 S_4} & \mathbf{K}_{S_4 V_3} \\ \mathbf{K}_{V_3 S_2} & \mathbf{K}_{V_3 S_4} & \mathbf{K}_{V_3 V_3} \end{bmatrix}^{-1} \begin{bmatrix} \mathbf{A}_2 & 0 \\ 0 & -\mathbf{A}_4 \\ 0 & 0 \end{bmatrix} \begin{bmatrix} \mathbf{c}_2 \\ \mathbf{c}_4 \end{bmatrix}. \quad (4.12)$$

By solving the linear system with the modal field excitations and extracting the field related to the apertures, one obtains

$$\begin{bmatrix} \mathbf{E}_{S_1} \\ \mathbf{E}_{S_3} \end{bmatrix} = \begin{bmatrix} \mathbf{x}_{11}^1 & \mathbf{x}_{12}^1 \\ \mathbf{x}_{21}^1 & \mathbf{x}_{22}^1 \end{bmatrix} \begin{bmatrix} \mathbf{c}_1 \\ \mathbf{c}_3 \end{bmatrix} \quad (4.13)$$

$$\begin{bmatrix} \mathbf{E}_{S_3} \\ \mathbf{E}_{S_4} \end{bmatrix} = \begin{bmatrix} \mathbf{x}_{11}^2 & \mathbf{x}_{12}^2 \\ \mathbf{x}_{21}^2 & \mathbf{x}_{22}^2 \end{bmatrix} \begin{bmatrix} \mathbf{c}_3 \\ \mathbf{c}_4 \end{bmatrix} \quad (4.14)$$

$$\begin{bmatrix} \mathbf{E}_{S_2} \\ \mathbf{E}_{S_4} \end{bmatrix} = \begin{bmatrix} \mathbf{x}_{11}^3 & \mathbf{x}_{12}^3 \\ \mathbf{x}_{21}^3 & \mathbf{x}_{22}^3 \end{bmatrix} \begin{bmatrix} \mathbf{c}_2 \\ \mathbf{c}_4 \end{bmatrix}, \quad (4.15)$$

where in  $\mathbf{x}_{i,j}^k$ ,  $i, j$  denote the local aperture numbers and  $k$  denotes the layer number.

To determine the four groups of the modal field coefficient for the four apertures in Figure 4.1, we need four equations. Two neighboring layers share the same aperture on their interface where the fields have to be identical. Therefore, we have two equations in the following

$$\mathbf{x}_{21}^1 \mathbf{c}_1 + (\mathbf{x}_{22}^1 - \mathbf{x}_{11}^2) \mathbf{c}_3 - \mathbf{x}_{12}^2 \mathbf{c}_4 = 0 \quad (4.16)$$

$$\mathbf{x}_{21}^3 \mathbf{c}_2 - \mathbf{x}_{21}^2 \mathbf{c}_3 + (-\mathbf{x}_{22}^2 + \mathbf{x}_{22}^3) \mathbf{c}_4 = 0. \quad (4.17)$$

The other two equations come from the port boundary condition

$$\hat{n} \times \nabla \times \mathbf{E} + \mathbf{P}(\mathbf{E}) = \mathbf{U}^{inc}. \quad (4.18)$$

By applying Galerkin's method and the finite element discretization to the port boundary condition, we have two equations associated with port 1 and

port 2, respectively

$$-\mathbf{A}_1 \mathbf{c}_1 + \mathbf{P}_1 \mathbf{E}_{S_1} = \mathbf{u}_{S_1} \quad (4.19)$$

$$-\mathbf{A}_2 \mathbf{c}_2 + \mathbf{P}_2 \mathbf{E}_{S_2} = \mathbf{u}_{S_2}. \quad (4.20)$$

Enforcing the equality of the electric field at ports, we have

$$(\mathbf{P}_1 \mathbf{x}_{11}^1 - \mathbf{A}_1) \mathbf{c}_1 + \mathbf{P}_1 \mathbf{x}_{12}^1 \mathbf{c}_3 = \mathbf{u}_{S_1} \quad (4.21)$$

$$(\mathbf{P}_2 \mathbf{x}_{11}^3 - \mathbf{A}_2) \mathbf{c}_2 + \mathbf{P}_2 \mathbf{x}_{12}^3 \mathbf{c}_4 = \mathbf{u}_{S_2}. \quad (4.22)$$

Till now, we have all the four equations as

$$(\mathbf{P}_1 \mathbf{x}_{11}^1 - \mathbf{A}_1) \mathbf{c}_1 + \mathbf{P}_1 \mathbf{x}_{12}^1 \mathbf{c}_3 = \mathbf{u}_{S_1} \quad (4.23)$$

$$\mathbf{x}_{21}^1 \mathbf{c}_1 + (\mathbf{x}_{22}^1 - \mathbf{x}_{11}^2) \mathbf{c}_3 - \mathbf{x}_{12}^2 \mathbf{c}_4 = 0 \quad (4.24)$$

$$(\mathbf{P}_2 \mathbf{x}_{11}^3 - \mathbf{A}_2) \mathbf{c}_2 + \mathbf{P}_2 \mathbf{x}_{12}^3 \mathbf{c}_4 = \mathbf{u}_{S_2} \quad (4.25)$$

$$\mathbf{x}_{21}^3 \mathbf{c}_2 - \mathbf{x}_{21}^2 \mathbf{c}_3 + (-\mathbf{x}_{22}^2 + \mathbf{x}_{22}^3) \mathbf{c}_4 = 0. \quad (4.26)$$

In the matrix form, the set of Equations (4.23-4.26) is

$$(\mathbf{P}\mathbf{M} - \mathbf{A}) \mathbf{c} = \mathbf{u}, \quad (4.27)$$

where

$$\mathbf{P} = \begin{bmatrix} \mathbf{P}_1 & 0 & 0 & 0 \\ 0 & \mathbf{P}_2 & 0 & 0 \\ 0 & 0 & \mathbf{I} & 0 \\ 0 & 0 & 0 & \mathbf{I} \end{bmatrix} \quad (4.28)$$

$$\mathbf{M} = \begin{bmatrix} \mathbf{x}_{11}^1 & 0 & \mathbf{x}_{12}^1 & 0 \\ 0 & \mathbf{x}_{11}^3 & 0 & \mathbf{x}_{12}^3 \\ \mathbf{x}_{21}^1 & 0 & \mathbf{x}_{22}^1 - \mathbf{x}_{11}^2 & -\mathbf{x}_{12}^2 \\ 0 & \mathbf{x}_{21}^3 & -\mathbf{x}_{21}^2 & -\mathbf{x}_{22}^2 + \mathbf{x}_{22}^3 \end{bmatrix} \quad (4.29)$$

$$\mathbf{A} = \begin{bmatrix} \mathbf{A}_1 & 0 & 0 & 0 \\ 0 & \mathbf{A}_2 & 0 & 0 \\ 0 & 0 & 0 & 0 \\ 0 & 0 & 0 & 0 \end{bmatrix} \quad (4.30)$$

$$\mathbf{c} = [\mathbf{c}_1 \quad \mathbf{c}_2 \quad \mathbf{c}_3 \quad \mathbf{c}_4]^T \quad (4.31)$$

$$\mathbf{u} = [\mathbf{u}_{S_1} \quad \mathbf{u}_{S_2} \quad 0 \quad 0]^T. \quad (4.32)$$

Multiplying both sides of Equation (4.27) by  $\tilde{\mathbf{A}}^H$  in the form of

$$\tilde{\mathbf{A}} = \begin{bmatrix} \mathbf{A}_1 & 0 & 0 & 0 \\ 0 & \mathbf{A}_2 & 0 & 0 \\ 0 & 0 & \mathbf{A}_3 & 0 \\ 0 & 0 & 0 & \mathbf{A}_3 \end{bmatrix} \quad (4.33)$$

results in a square system of modal coefficients

$$\tilde{\mathbf{A}}^H (\mathbf{P}\mathbf{M} - \mathbf{A}) \mathbf{c} = \tilde{\mathbf{A}}^H \mathbf{u}. \quad (4.34)$$

All the modal coefficients can be solved through Equation (4.34), and all of the aperture fields can be obtained via the interface systems of Equation (4.13), Equation (4.14), and Equation (4.15).

## 4.2 The Approximate Modal Interface Method and the Solution Space Projection

It is observed that the most time-consuming part is the process of building the modal coefficient matrix in Equation (4.34) rather than solving it. In building Equation (4.34) upon the quest of a broadband analysis, one needs to solve the linear system of equations associated with each layer at many frequency sampling points. Moreover, a single mode is generally insufficient to expand the fields on an aperture, and in order to maintain a certain accuracy, it is necessary to utilize multiple modes. Therefore, it requires matrix factorization for every single layer at every frequency sampling point, and at the same time solving for multiple right-hand sides  $\mathbf{a}_{i,k}$  (excitation of  $k^{th}$  mode at aperture  $i$ ). In this section, we attempt to generate reduced-order models for individual layers such that the process of constructing the modal coefficient matrices can be accelerated over a broadband.

The method of solution space projection introduced in Chapter 3 is excitation-dependent, which introduces more than one ways to build the reduced-order models. One of the approaches is to build the reduced-order model based on each single-mode excitation at one aperture. For example, there are apertures  $S1$  and  $S3$  in the top layer as shown in Figure 4.1, and suppose that the field at each aperture is expanded by three modes. The total number of six excitations will create six reduced-order models for a single layer. This process will become cumbersome when we have thousands of via-holes and we have to deal with thousands of reduced-order models simultaneously. It seems not the best choice of associating one reduced-order model with a single-mode excitation. Another approach is to build a single reduced-order model for each layer by lumping all the solution vectors from all the modal excitations in that layer. It takes fewer sampling frequency points to build this kind of reduced-order model since the latter contains more information per sampling frequency. However, this turns out to be inefficient since it takes a considerable amount of time and memory in orthonormalizing the solution vectors to obtain a set of orthonormal basis. After filtering out the two extremes cases, it ends up with a balanced option. All the via-holes sitting on the same interface will have one reduced-order model; ports in the same layer will contribute to the same reduced-order model. In this case, we will have maximum three reduced-order models per layer, namely, one

associated with excitations on the upper interface, one with excitations on the lower interface, and one with the wave port excitations.

The following part will illustrate the process of the adaptive multi-point solution space projection scheme under the approximate modal interface method. Again, taking the top layer of Figure 4.1 as an example and re-writing Equation 4.10 into a more compact form, we have

$$\begin{aligned}
\begin{bmatrix} \mathbf{E}_{S_1} \\ \mathbf{E}_{S_3} \\ \mathbf{E}_{V_1} \end{bmatrix} &= \begin{bmatrix} \mathbf{K}_{S_1 S_3} & 0 & \mathbf{K}_{S_1 V_1} \\ 0 & \mathbf{K}_{S_3 S_3} & \mathbf{K}_{S_3 V_1} \\ \mathbf{K}_{V_1 S_1} & \mathbf{K}_{V_1 S_3} & \mathbf{K}_{V_1 V_1} \end{bmatrix}^{-1} \begin{bmatrix} \mathbf{A}_1 & 0 \\ 0 & \mathbf{A}_3 \\ 0 & 0 \end{bmatrix} \begin{bmatrix} \mathbf{c}_1 \\ \mathbf{c}_3 \end{bmatrix} \\
&= \mathbf{K}^{-1} \begin{bmatrix} \mathbf{a}_1 & \mathbf{a}_3 \end{bmatrix} \begin{bmatrix} \mathbf{c}_1 \\ \mathbf{c}_3 \end{bmatrix} \\
&= \begin{bmatrix} \mathbf{x}_1 & \mathbf{x}_3 \end{bmatrix} \begin{bmatrix} \mathbf{c}_1 \\ \mathbf{c}_3 \end{bmatrix}. \tag{4.35}
\end{aligned}$$

The top layer in Figure 4.10 does not have apertures on the upper interface, and we will have only two reduced-order models for that layer. There will be one reduced-order model associated with all the ports in the top layer, to be specific, the port surface  $S_1$ , and another reduced-order model with apertures sitting on the lower interface, namely,  $S_3$ . Certainly for the cases with more apertures in the layer, the extra apertures will contribute to either the port reduced-order model or the lower interface reduced-order model accordingly. The reduced-order model associated with  $S_1$  is built upon adaptively by solving  $\mathbf{K}\mathbf{x}_1 = \mathbf{a}_1$ . After a number of sampling frequencies the residual drops below the preset tolerance and we can arrange the solution vectors of different frequencies column-wise as

$$\mathbf{X} = \begin{bmatrix} \mathbf{x}_1(k_1) & \mathbf{x}_1(k_2) & \dots & \mathbf{x}_1(k_{N_s}) \end{bmatrix}. \tag{4.36}$$

Orthonormalizing  $\mathbf{X}$  to  $\mathbf{H}$  and projecting the original problem onto the space spanned by the column vectors of  $\mathbf{H}$ , one obtains

$$\mathbf{H}^H \mathbf{K}(k) \mathbf{H} \mathbf{y} = \mathbf{H}^H \mathbf{a}_1(k), \tag{4.37}$$

and the solution of the original problem can be recovered by  $\mathbf{x}(k) = \mathbf{H} \mathbf{y}$ .

It is worth mentioning that the strategy of checking convergence is slightly different from that in Chapter 3. Since it is the unknowns on the aperture

that are to be used in constructing the modal coefficient matrix, only those entries need to be checked by the residual defined as

$$\boldsymbol{r} = \frac{|\boldsymbol{a}_1(k, \text{DOF}_a) - \boldsymbol{K}(k, \text{DOF}_a)\boldsymbol{x}(k, \text{DOF}_a)|}{|\boldsymbol{a}_1(k, \text{DOF}_a)|}, \quad (4.38)$$

where  $\text{DOF}_a$  denotes the unknowns associated with the apertures.

### 4.3 Domain Decomposition within Layers: The Finite Element Tearing and Interconnecting

As the decomposition of domains is performed over layers and through the expansion and re-coupling of the modal fields of the apertures on the layer interfaces, the approximate modal interface method is seemingly predestined as a one-way domain decomposition. Even though the layers can be thoroughly decoupled, the approximate modal interface methods find limitations in a few ways. Generally the size of a single layer in most of the practical problems can still be considerably large, and factorizing the linear system of huge dimension may require a tremendous amount of time and memory resource. Other than that, most of times we encounter unbalanced domains since the top and bottom layers are usually open structures truncated with absorbing boundaries, and the thicknesses of the multiple dielectric layers and metal planes are nonuniform. The existence of unbalanced layers is likely to degrade the parallel computing efficiency. Therefore, in this section, we seek the possibility of two-way domain decomposition, which will not only decompose the computational domain by layers but also within each layer. The two-way domain decomposition with its generality and flexibility seems a good remedy to account for the problems appearing in the one-way domain decomposition. In this section, we use the method of the finite element tearing and interconnecting to further cut each layer into a number of subdomains.

#### 4.3.1 Finite Element Tearing and Interconnecting

The finite element tearing and interconnecting method has been applied to solve large-scale three-dimensional electromagnetic problems in [14]. Fol-

lowing the convention in [14], the finite element tearing and interconnecting will be denoted as FETI-DPEM. By applying the FETI-DPEM method, one single layer is torn into  $N_s$  non-overlapping subdomains. The neighboring subdomains  $\Omega^i$  and  $\Omega^j$  share the interface denoted as  $\Gamma_{ij}$ . To enforce the tangential continuity of the electric field at the interfaces, the Dirichlet-type transmission condition

$$\hat{n}^i \times \hat{n}^i \times \mathbf{E}^i = \hat{n}^j \times \hat{n}^j \times \mathbf{E}^j \quad (4.39)$$

and the Neumann-type transmission condition

$$\hat{n}^i \times \frac{1}{\mu^i} \nabla \times \mathbf{E}^i = -\hat{n}^j \times \frac{1}{\mu^j} \nabla \times \mathbf{E}^j = \mathbf{\Lambda} \quad (4.40)$$

are enforced simultaneously. In Equation (4.39) and Equation (4.40),  $\hat{n}^i$  is the unit normal vector at the interface  $\Gamma_{ij}$  pointing from subdomain  $i$  to the exterior region, and  $\mathbf{\Lambda}$  is the Neumann boundary data, which is unknown.

The finite element discretization is applied to individual subdomains, and the discretization of the Neumann-type transmission condition results in the term

$$(\mathbf{B}^s)^T \lambda = \int_{\Gamma^s} \mathbf{N}^s \cdot \mathbf{\Lambda} dS, \quad (4.41)$$

where  $\mathbf{B}^s$  is a signed boolean matrix that extracts the interface DOFs of the  $s^{th}$  subdomain. Also,  $\lambda$  is the dual variable, called the Lagrange multiplier.

By using the Lagrange multiplier, the continuity is enforced at the subdomain interfaces. Taking account of other boundary conditions, the linear system of individual subdomain becomes

$$\mathbf{K}^s + (\mathbf{B}^s)^T \lambda = \mathbf{f}^s, \quad (4.42)$$

where  $(\mathbf{B}^s)^T \lambda$  includes the information of the subdomain interfaces of the  $s^{th}$  subdomain,  $\mathbf{K}^s$  includes the volumetric discretization information of the  $s^{th}$  subdomain other than the subdomain interfaces, and  $\mathbf{f}^s$  contains the information of the excitation in the  $s^{th}$  subdomain. Similarly we can have the system equations for all the subdomains and rearrange them into a global system as follows

$$\begin{bmatrix} \mathbf{K}^1 & \dots & 0 & (\mathbf{B}^1)^T \\ \vdots & \ddots & \vdots & \vdots \\ 0 & \dots & \mathbf{K}^{N_s} & (\mathbf{B}^{N_s})^T \\ \mathbf{B}^1 & \dots & \mathbf{B}^{N_s} & 0 \end{bmatrix} \begin{bmatrix} \mathbf{E}^1 \\ \vdots \\ \mathbf{E}^{N_s} \\ \lambda \end{bmatrix} = \begin{bmatrix} f^1 \\ \vdots \\ f^{N_s} \\ 0 \end{bmatrix}. \quad (4.43)$$

It is worth mentioning that the last equation in Equation (4.43) is the contribution from the Dirichlet-type boundary condition. By eliminating  $\mathbf{E}^s$ ,  $s = 1, 2, \dots, N_s$ , we arrive at an interface system of  $\lambda$

$$\mathbf{F}\lambda = d, \quad (4.44)$$

where

$$\mathbf{F} = \sum_{s=1}^{N_s} \mathbf{B}^s (\mathbf{K}^s)^{-1} (\mathbf{B}^s)^T \quad (4.45)$$

$$d = \sum_{s=1}^{N_s} \mathbf{B}^s (\mathbf{K}^s)^{-1} f^s. \quad (4.46)$$

The interface system in Equation (4.44) can be solved using Krylov subspace methods such as the generalized minimum residual (GMRES) method and biconjugate gradient stabilized (BiCGSTAB) method together with the Dirichlet preconditioner [20]. The Dirichlet preconditioner offers a good approximation of the inverse of  $\mathbf{F}$  in Equation (4.44) as

$$\mathbf{F}^{-1} = \sum_{s=1}^{N_s} \mathbf{B}^s \begin{bmatrix} 0 & 0 \\ 0 & \mathbf{S}_{II}^s \end{bmatrix} (\mathbf{B}^s)^T, \quad (4.47)$$

where

$$\mathbf{S}_{II}^s = \mathbf{K}_{II}^s - \mathbf{K}_{IV}^s (\mathbf{K}_{VV}^s)^{-1} (\mathbf{K}_{IV}^s)^T \quad (4.48)$$

and the subscripts  $V$  and  $I$  denote the volume and interface unknowns, respectively.

The original problem is reduced to an interface problem of a much smaller dimension. After iteratively solving the interface problem for the dual variables, the field unknowns can be extracted with the obtained Neumann-type

boundary condition for individual subdomains.

## 4.4 The Finite Element Tearing and Interconnecting and the Solution Space Projection

The incorporation of the solution space projection into the FETI-DPEM method is straightforward. Since the original problem is solved intermediately through the interface problem, the field coefficient can be recovered through the known dual variables and all the other given boundary conditions. The field solutions from all the subdomains can be lumped into one global solution vector. With the global solution vector, one can refer to the steps in Chapter 2 to build the reduced-order models. Therefore, the only difference of the FETI-DPEM and SSP from the FEM and SSP is the intermediate step of recovering the field coefficients from the subdomain interface problem.

## 4.5 Numerical Examples

### 4.5.1 Through-Hole Via Structure

The first example is the same as that shown in Figure 3.16, which is a through-hole via structure of three dielectric layers separated by two conducting planes. Owing to the existence of the two metal planes, the multilayer interconnect can be divided into three individual subdomains each associated with one layer. Other than directly using the finite element method, this section employs the method of approximate modal interface and the method of finite element tearing and interconnecting. The method of solution space projection has also been incorporated to obtain the results in Figures 4.2 and 4.3. Figures 4.2 and 4.3 show a good match of S-parameters among the results obtained by directly using the finite element method, AMI, and FETI-DPEM. This example validates the implementation of the approximate modal interface method and the finite element tearing and interconnecting method.

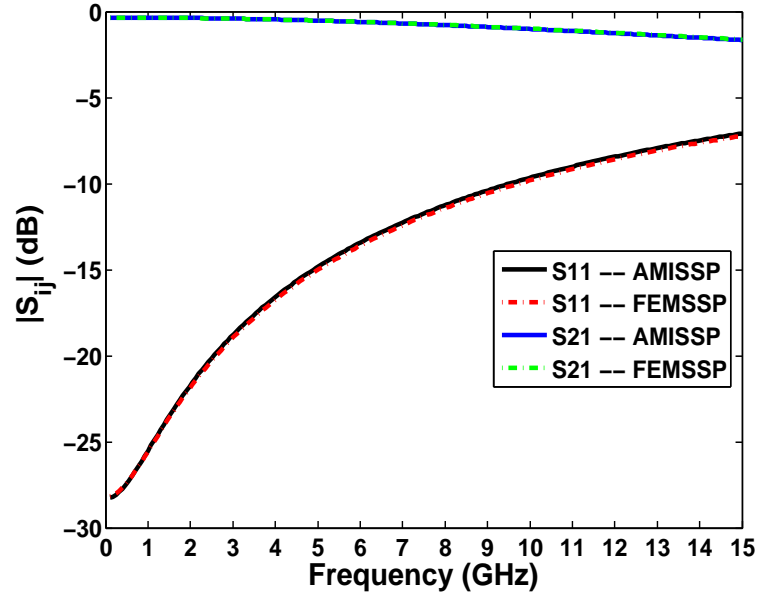


Figure 4.2:  $S_{11}$  and  $S_{12}$  of the through-hole via structure

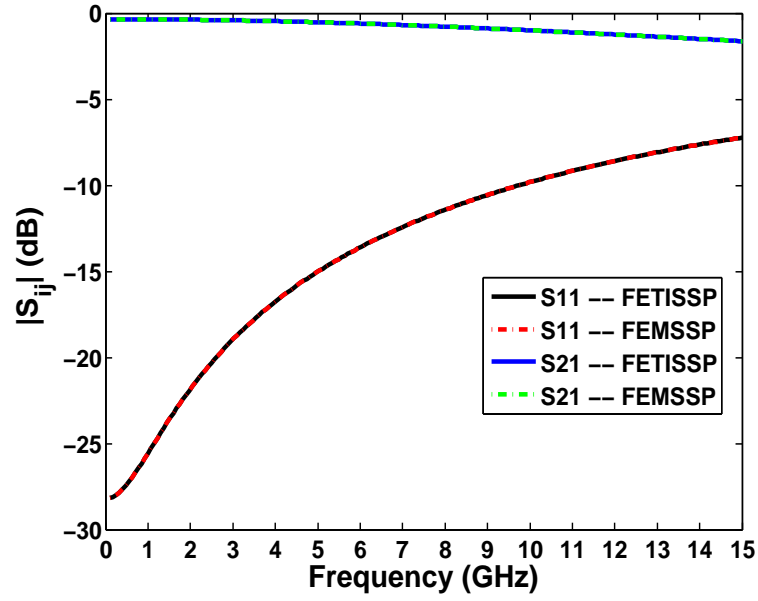


Figure 4.3:  $S_{11}$  and  $S_{12}$  of the through-hole via structure

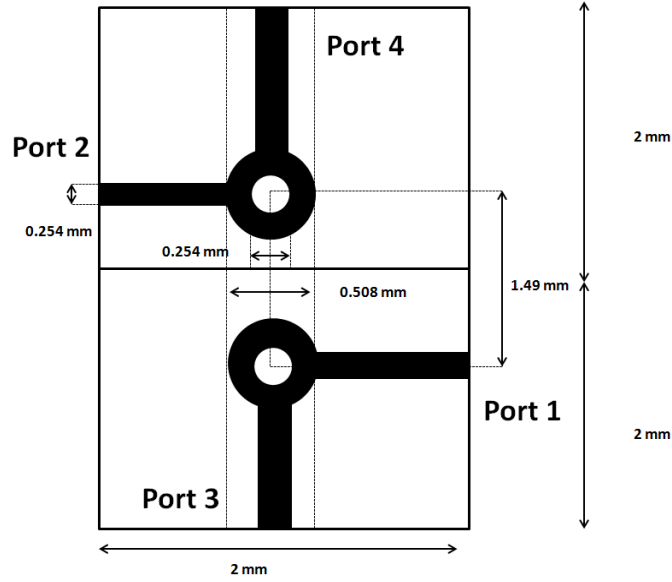


Figure 4.4: Top view of a three-layered interconnect with coupled signal traces

#### 4.5.2 Multilayer Interconnect with Bending Signal Traces

In this example, coupled signal traces come in on the first layer and branch out at the bottom layer where the planar directions of in- and out-signal traces are perpendicular to each other. The stack-up of this example is the same as that shown in Figure 3.16. Figure 4.4 illustrates the detailed information of the layout: the width of all the microstrip lines is 0.254 mm; the antipad shares the same diameter with the pad, both of which are 0.508 mm; the diameter of the drilled via hole is 0.254 mm; and the separation of the two coupled vias is 1.49 mm.

Similar to the previous example, the method of approximate interface method cuts the entire structure into three layers. In the simulation with the method of finite element tearing and interconnecting, each layer is further cut into two subdomains, each of which forms a square of  $2 \text{ mm} \times 2 \text{ mm}$ . It is also worth mentioning that the port 1 and port 2 are on the top layer and port 3 and port 4 are on the bottom layer. The S-parameters of this three-layered structure is shown in Figures 4.5 and 4.6 with directly using the finite element method, applying AMI to cut into layers, and two-way domain decomposition with FETI-DPEM. It can be seen that the results from all the three method are identical.

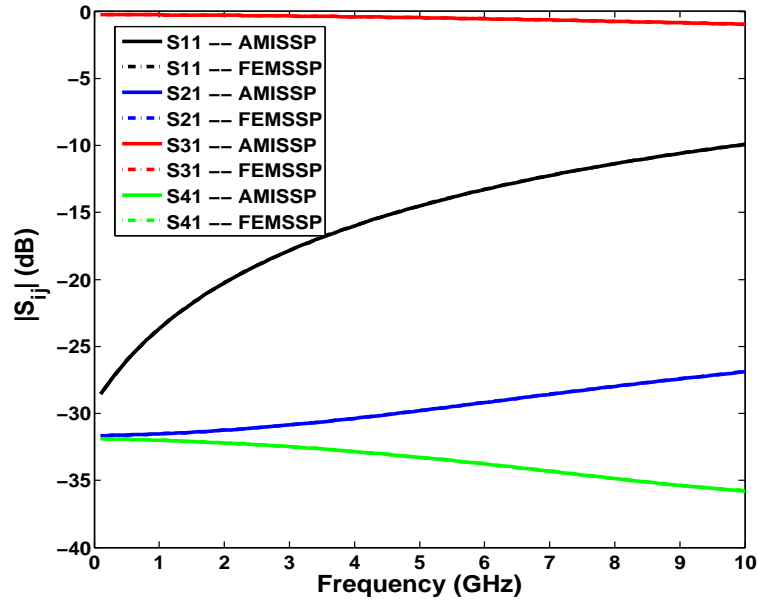


Figure 4.5: S-parameters of the three-layered interconnect with coupled signal traces by direct FEM and AMI

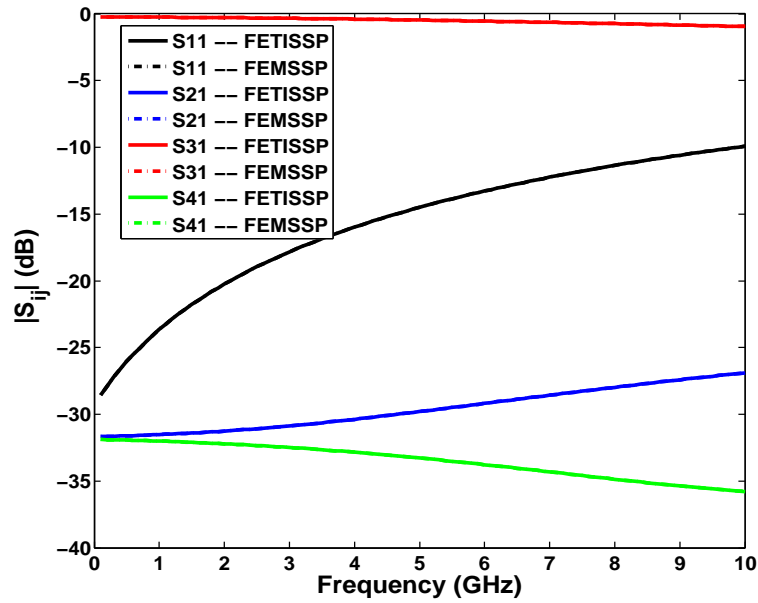


Figure 4.6: S-parameters of the three-layered interconnect with coupled signal traces by direct FEM and FETI-DPEM

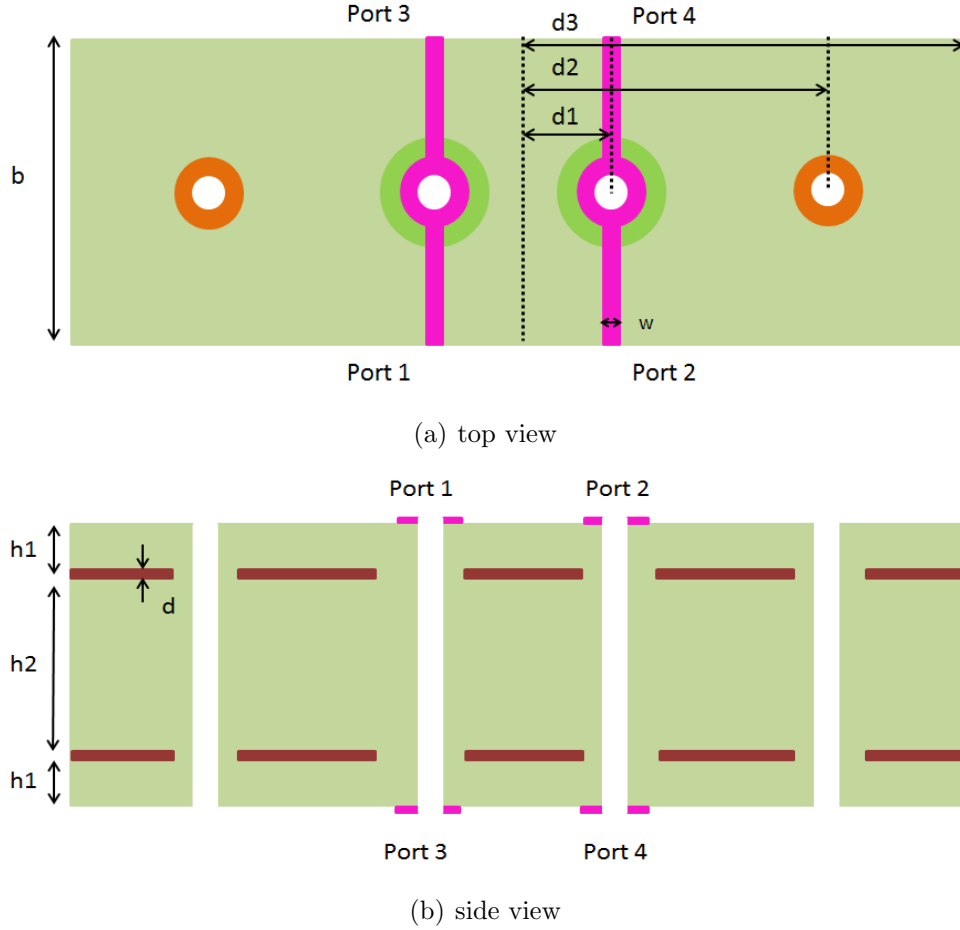


Figure 4.7: Three-layered interconnect with stitching vias

### 4.5.3 Multilayer Interconnect with and without Stitching Vias

The examples in this subsection investigate the via stitching impact on the signal integrity of the multilayer interconnects. As we know the multiple power and ground planes in the multilayer interconnect act as microstrip-patch antennas and result in radiations due to the fringing fields at the board edges. The radiations are essential to some undesirable couplings inside the structure and most likely to create signal integrity issues. To mitigate this kind of radiation, stitching the ground planes together at the periphery of the board using closely spaced vias has been proposed. It has been shown that the via stitching can effectively reduce the undesirable radiation from the fringing fields at the edge of the board [21]. As shown in Figure 4.7, coupled microstrip lines on the top and bottom layers are connected through vias. The radii of barrel, pad, and antipad are 5 mil, 10 mil, and 15 mil,

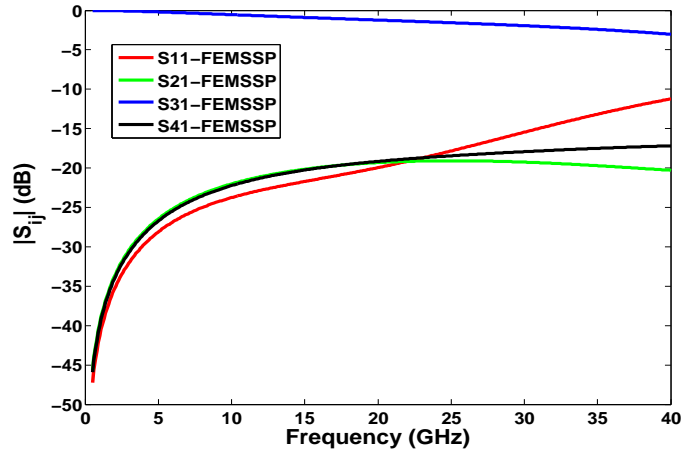
respectively. As in Figure 4.7(b), the width of the microstrip lines is 5 mil. The metal layer has a thickness of  $d = 0.7$  mil. The top and bottom dielectric layers have a thickness of  $h1 = 3$  mil, and the middle dielectric layer has a thickness of  $h2 = 20$  mil. The relative permittivity of the dielectric layers is  $\epsilon_r = 4.2$  with a loss tangent of 0.01.

#### 4.5.3.1 Stitching Vias with a Separation of 120 mil

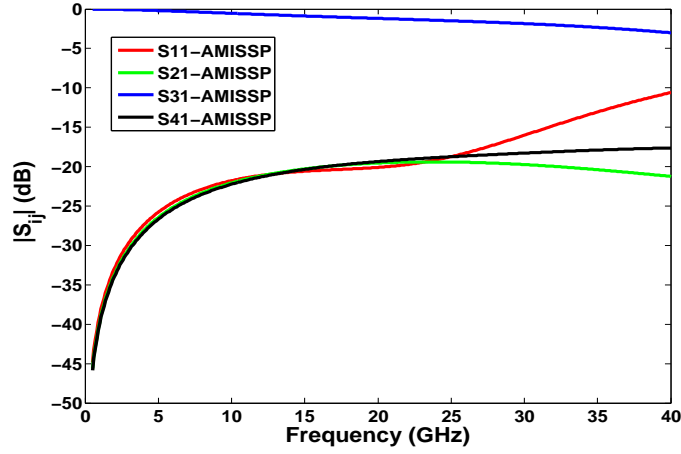
In this case, the distances shown in Figure 4.7(a) are as follows:  $d1 = 20$  mil,  $d2 = 60$  mil, and  $d3 = 120$  mil. The S-parameters of this structure are shown in Figure 4.8(a) with directly using FEM, Figure 4.8(b) with the method of AMI, and Figure 4.8(c) with the method of FETI-DPEM. By using the method of AMI, the entire structure is separated into three layers. With the method of FETI-DPEM, each layer is further cut into four subdomains. The frequency band has a range from 0.5 GHz to 40 GHz, and 400 samples are employed. The results from all the three methods match very well with each other. With the solution space projection, only seven frequency points are used to construct the reduced-order model with both direct FEM and FETI-DPEM.

#### 4.5.3.2 Stitching Vias with a Separation of 240 mil

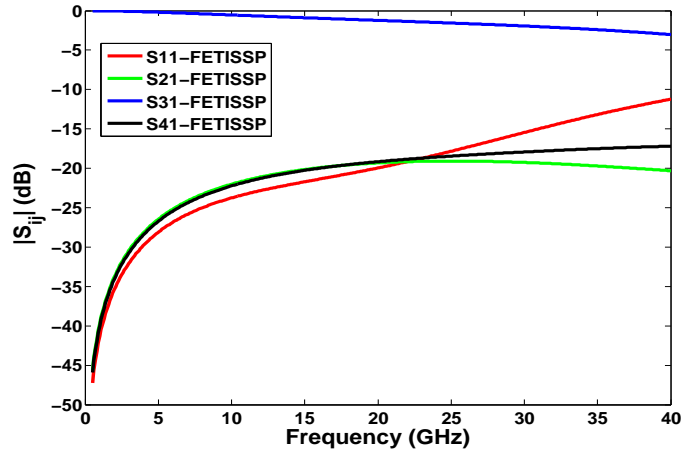
In this case, the distances shown in Figure 4.7(a) are as follows:  $d1 = 20$  mil,  $d2 = 120$  mil, and  $d3 = 160$  mil. The S-parameters of this structure are shown in Figure 4.9(a) with directly using FEM, Figure 4.9(b) with the method of AMI, and Figure 4.9(c) with the method of FETI-DPEM. Similar to the previous case, with the method of FETI-DPEM, each layer is further cut into four subdomains. The frequency band has a range from 0.5 GHz to 40 GHz, and 400 samples are employed. The results from all the three methods seems identical. With the solution space projection, only seven frequency points are used to construct the reduced-order model with both direct FEM and FETIDP.



(a) result with FEM and SSP

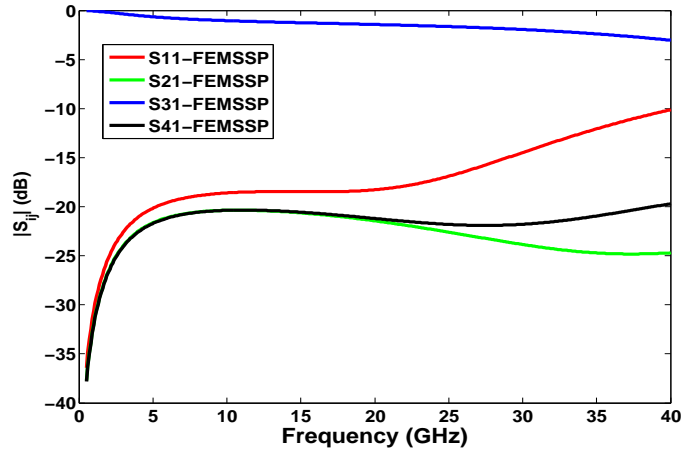


(b) result with AMI and SSP

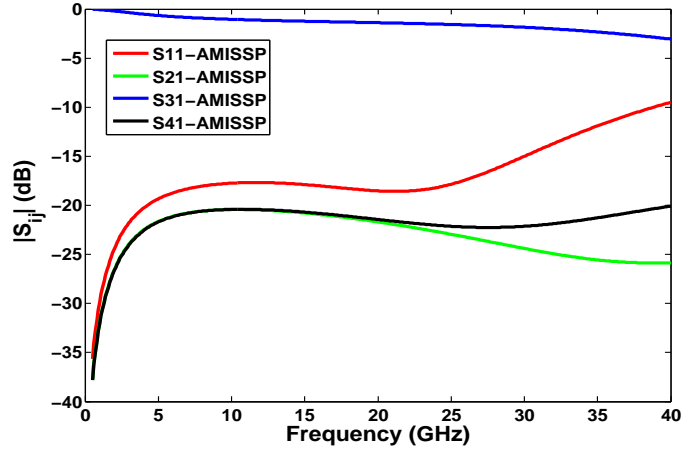


(c) result with FETI-DPEM and SSP

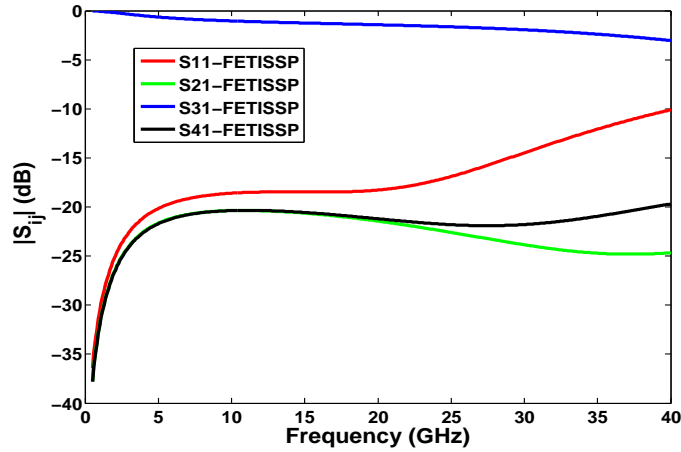
Figure 4.8: S-parameter of the three-layered interconnect with stitching vias (separation of 120 mil)



(a) result with direct FEM and SSP

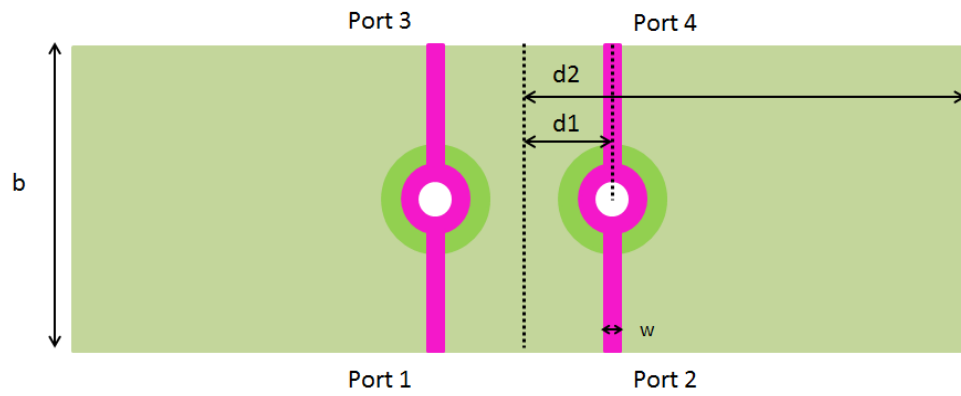


(b) result with AMI and SSP

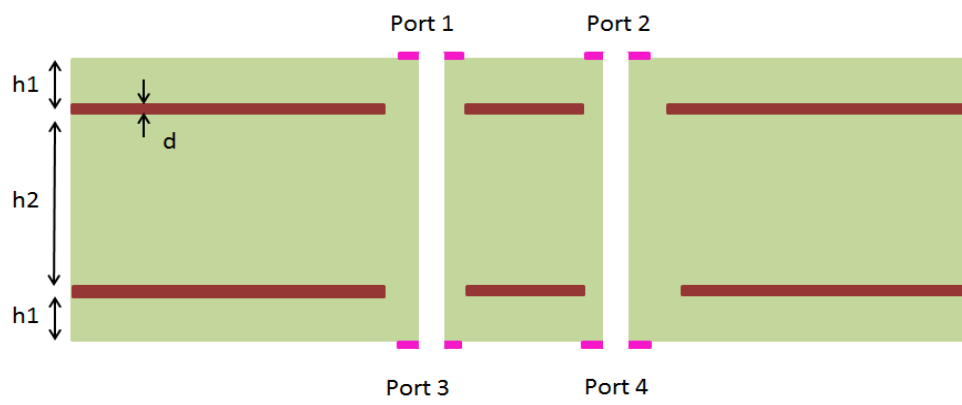


(c) result with FETI-DPEM and SSP

Figure 4.9: S-parameter of the three-layered interconnect with stitching vias (separation of 240 mil)



(a) top view

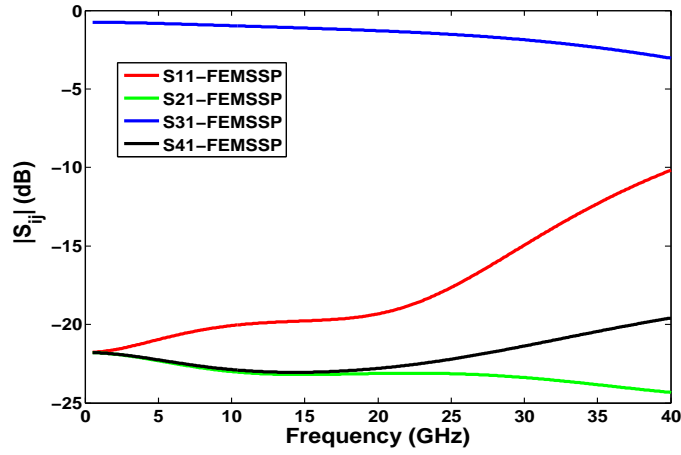


(b) side view

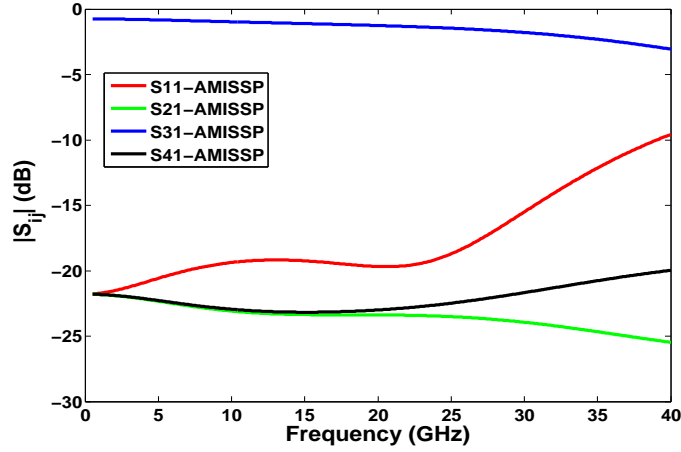
Figure 4.10: Three-layered interconnect with stitching vias

#### 4.5.4 No Stitching Via

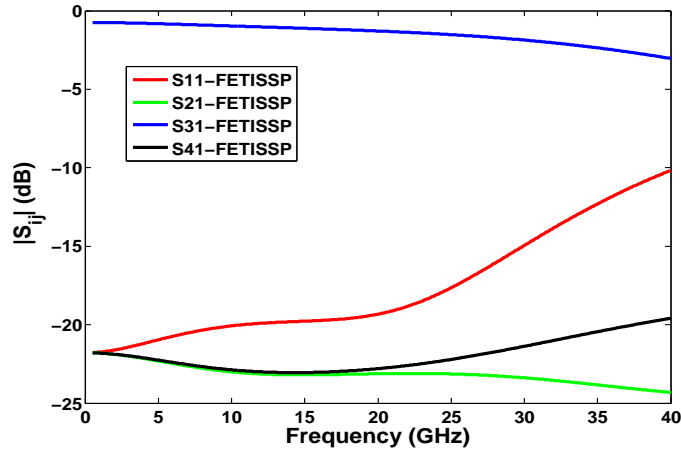
The stitching vias are removed in this case. The distances shown in Figure 4.10(a) are  $d1 = 20$  mil and  $d2 = 60$  mil. The S-parameters of this structure are shown in Figure 4.11(a) with directly using FEM, Figure 4.11(b) with the method of AMI, and Figure 4.11(c) with the method of FETI-DPEM. By using the method of AMI, the entire structure is separated into three layers. With the method of FETI-DPEM, each layer is further cut into two subdomains. The frequency band has a range from 0.5 GHz to 40 GHz, and 400 samples are employed. The results from all the three methods match very well with each other. With the solution space projection, only seven frequency points are used to construct the reduced-order model with both direct FEM and FETI-DPEM.



(a) result with direct FEM and SSP



(b) result with AMI and SSP



(c) result with FETI-DPEM and SSP

Figure 4.11: S-parameter of the three-layered interconnect without stitching vias

# CHAPTER 5

## CONCLUSION

In this work, a three-dimensional full-wave solver based on the finite element method is implemented as a tool to perform the signal integrity analysis of high-speed multilayer interconnects. Wave ports are incorporated into the full-wave solver to mimic the circuit excitations and truncate an infinite computational domain. The wave port is based on a two-dimensional eigen-solver at the port surfaces which is responsible of extracting a certain number of propagation modes and evanescent modes upon request. The three-dimensional full-wave solver is capable of solving various circuit problems as demonstrated in the numerical examples.

There are mainly two categories of approaches of modeling the high-speed multilayer interconnects. Compared to the circuit models based on circuit-parameter extractions, full-wave methods are generally computational intensive. In order to speed up the design process and maintain certain accuracies, fast and efficient full-wave solvers are most desirable. Therefore, methods to enhance the efficiency of the full-wave solvers are investigated and implemented in this work, namely, the method of solution space projection and the domain decomposition schemes.

The method of solution space projection assists the full-wave solver in achieving a fast frequency sweep. Over a broadband analysis of the multilayer interconnects, the same problem has to be solved repeatedly at many frequency samples, leading to a huge computation burden. By utilizing the information at only a few frequency samples and projecting the original problem into the subspace spanned by the information at few selected frequency samples, the method of solution space projection produces a reduced-order model which has a much smaller dimension than the original problem but is capable of yielding accurate predictions as the original problem does. The adaptive and multi-point nature of the solution space projection prevents the redundancy in the information collected to form the reduced-order mo-

del. The efficiency of the full-wave solver with the solution space projection has been demonstrated with various numerical examples.

Domain decomposition schemes uncover another possibility on enhancing the efficiency of the full-wave analysis. The original problem is broken into a few smaller ones and this idea allows the possibility of parallel computing. Two domain decomposition schemes are investigated here, namely, the method of approximate modal interface and the method of finite element tearing and interconnecting. The approximate modal interface method is a one-way domain decomposition scheme and it performs the domain decomposition by layers, to be specific, one layer forms one subdomain. The approximate interface method utilizes the modal solutions at the apertures shared by two adjacent layers to realize the decomposition and re-couple among the subdomains. The other domain decomposition scheme presented in this work is the method of finite element tearing and interconnecting. This method is able to perform domain decomposition even within layers and is considered as a two-way domain decomposition. By introducing the Dirichlet-type and Neumann-type boundaries on the subdomain interfaces, the original problem is first divided into a number of subdomains and then transformed into a subdomain interface problem of a much smaller dimension. The solutions of the original problems can be recovered in subdomain wise after solving the subdomain interface problem. Finally, the proposed solution space projection and the domain decomposition schemes are combined in a mutually beneficial manner by which we may be able to come up with an even faster and more efficient full-wave method.

## REFERENCES

- [1] A. E. Ruhli and A. C. Cagellaris, "Progress in the methodologies for the electrical modeling of interconnects and electronic packages," *Proc. IEEE*, vol. 89, pp. 740–771, 2001.
- [2] R. Achar and M. S. Nakhla, "Simulation of high-speed interconnects," *Proc. IEEE*, vol. 89, pp. 693–728, 2001.
- [3] E. P. Li, E. X. Liu, L. W. Li, and M. S. Leong, "A coupled efficient and systematic full-wave time-domain macromodeling and circuit simulation method for signal integrity analysis of high-speed interconnects," *IEEE Trans Advanced Packaging*, vol. 27, pp. 213–223, 2004.
- [4] H. J. Liaw, "Characterization and modeling of multilayer interconnections for high speed digital systems," Ph.D. dissertation, University of Illinois at Urbana-Champaign, 1996.
- [5] Y. Shao, Z. Peng, and J. F. Lee, "Signal integrity analysis of high-speed interconnects by using nonconformal domain decomposition method," *IEEE Trans Components, Packaging and Manufacturing Technology*, vol. 2, pp. 122–130, 2012.
- [6] J. Wang and R. Mittra, "Finite element analysis of MMIC structures and electronic packages using absorbing boundary conditions," *IEEE Trans. Microw. Theory Tech*, vol. 42, no. 3, pp. 441–449, 1994.
- [7] G. W. Pan, J. Tan, and B. K. Gilbert, "Full wave edge element based analysis of 3D metal-dielectric structures for high clock rate digital and microwave applications," *IEEE Proc. Microw. Antennas Propag*, vol. 147, no. 5, pp. 391–397, 2000.
- [8] W. D. Becker, P. H. Harms, and R. Mittra, "Time-domain electromagnetic analysis of interconnects in a computer chip package," *IEEE Trans. Microw. Theory Tech*, vol. 40, no. 12, pp. 2155–2163, 1992.
- [9] P. Cherry and M. F. Iskander, "FDTD analysis of high frequency electronic interconnection effects," *IEEE Trans. Microw. Theory Tech*, vol. 43, no. 10, pp. 2445–2451, 1995.

- [10] M. R. Abdul-Gaffoor, H. K. Smith, A. A. Kishk, and A. W. Glisson, "Simple and efficient full-wave modeling of electromagnetic coupling in realistic RF multilayer PCB layouts," *IEEE Trans. Microw. Theory Tech*, vol. 50, no. 6, pp. 1445–1457, 2002.
- [11] S. G. Hsu and R. B. Wu, "Full-wave characterization of a through hole via in multilayered packaging," *IEEE Trans. Microw. Theory Tech*, vol. 43, no. 5, pp. 1073–1081, 1995.
- [12] S. H. Lee and J. M. Jin, "Adaptive solution space projection for fast and robust wideband finite-element simulation of microwave components," *IEEE Microwave Wireless Component Letter*, vol. 17, no. 7, pp. 474–476, 2007.
- [13] S. H. Lee, K. Mao, and J. M. Jin, "A complete finite element analysis of multilayer anisotropic transmission lines from DC to terahertz frequencies," *IEEE Trans. Adv. Packag.*, vol. 31, no. 2, pp. 326–338, 2008.
- [14] Y. Li and J. M. Jin, "A vector dual-primal finite element tearing and interconnecting method for solving 3-D large-scale electromagnetic problems," *IEEE Trans Antennas Propag*, vol. 54, no. 10, pp. 3000–3009, 2006.
- [15] J. Liu, J.-M. Jin, E. K. N. Yung, and R. S. Chen, "A fast, higher order three-dimensional finite-element analysis of microwave waveguide devices," *Microwave Optic. Tech. Lett.*, vol. 32, no. 5, pp. 344–352, 2005.
- [16] J. M. Jin, *The Finite Element Method in Electromagnetics*. New York: John Wiley & Sons, 2002.
- [17] K. L. Wu and H. Y. Wang, "A rigorous modal analysis of h-plane waveguide t-junction loaded with a partial-height post for wideband applications," *IEEE Trans Microwave Theory Tech*, vol. 46, pp. 1721–1734, 1998.
- [18] D. M. Sheen, S. M. Ali, M. D. Abouzahra, and J. A. Kong, "Application of the three-dimensional finite-difference time-domain method to the analysis of planar microstrip circuits," *IEEE Trans Microwave Theory Tech*, vol. 38, no. 7, pp. 1712–1717, 1990.
- [19] S. Maeda, T. Kashiwa, and I. Fukai, "Full wave analysis of propagation characteristics of a through hole using the finite-difference time-domain method," *IEEE Trans Microwave Theory Tech*, vol. 39, pp. 2154–2159, 1991.
- [20] D. Rixen and C. Farhat, "A simple and efficient extension of a class of substructure based preconditioners to heterogeneous structural mechanics problems," *Int. J. Numer. Methods Eng.*, vol. 44, pp. 489–516, Feb. 1999.

- [21] X. Ye, D. M. Hochanson, M. Li, Y. Ren, W. Cui, J. L. Drewniak, and R. E. EuBroff, “EMI mitigation with multilayer power-bus stacks and via stitching of reference planes,” *IEEE Trans Electromagnetic compatibility*, vol. 43, no. 4, pp. 538–548, 2001.